

10299  
NACA TN 3964

TECH LIBRARY KAFB, NM  
0062010

# NATIONAL ADVISORY COMMITTEE FOR AERONAUTICS

TECHNICAL NOTE 3964

THE LINEARIZED SUBSONIC FLOW ABOUT SYMMETRICAL  
NONLIFTING WING-BODY COMBINATIONS

By John B. McDevitt

Ames Aeronautical Laboratory  
Moffett Field, Calif.



Washington  
April 1957



0067010

## NATIONAL ADVISORY COMMITTEE FOR AERONAUTICS

## TECHNICAL NOTE 3964

THE LINEARIZED SUBSONIC FLOW ABOUT SYMMETRICAL  
NONLIFTING WING-BODY COMBINATIONS

By John B. McDevitt

## SUMMARY

Methods are presented for determining the linearized subsonic flow about symmetrical, nonlifting wing-body combinations. The wing is represented by a suitable planar distribution of elementary sources in accordance with the usual assumptions of linearized, thin-airfoil theory. The required boundary condition for tangential flow at the body surface is met by distributing along the body axis suitable distributions of three-dimensional sources and multipoles. As part of the present analysis, a theory is presented for determining the flow about circular or noncircular bodies by the use of axially distributed sources and multipoles. The flow over thin, nonlifting airfoils having symmetrical profiles is also studied in considerable detail, and it is shown that the concept of the oblique source filament can be used in obtaining numerical results for wings having tapered as well as untapered plan forms.

A comparison of theory and experiment is made for two  $45^\circ$  sweptback wings in combination with basic Sears-Haack bodies of revolution and in combination with the basic bodies indented according to Whitcomb's transonic area rule. The effect of indenting the body on the pressure distribution near the wing-body juncture is of particular interest for swept-wing and body combinations. The effect of the area-rule indentation was to adjust the pressure field near the body so that the wing surface isobars tended to follow the local sweep lines of the wing.

## INTRODUCTION

Linearized theories for predicting the subsonic pressure distributions on thin wings or slender bodies have been developed in considerable detail but comparatively little attention has been directed toward the problem of predicting the subsonic pressure distributions on wings and bodies in combination. The existing theories for determining the subsonic flow about wing-body combinations are based on the assumption of extremely slender wings and bodies in accordance with the basic concepts of slender-body theory as initiated by Max Munk and R. T. Jones (refs. 1 and 2) and extended by numerous authors (see, in particular, refs. 3 to 6).

In the present paper the fundamental solutions of linearized, three-dimensional-flow theory are used in the development of a practical method for calculating the subsonic flow about nonlifting wing-body combinations. (The use of linearized theory requires, of course, that the wing be thin and the body slender but does not require the assumption of extreme slenderness involved in slender-body theory.) In the present method particular emphasis is placed on the practical application of the theory. No attempt is made to estimate the accuracy of calculated results using this method but a comparison of theory and experiment is provided.

In the analysis which follows, general relationships are first derived for determining the strengths of the wing planar sources and the singularities at the body center line so as to satisfy the required boundary condition for tangential flow at the wing-body surface. Next, the body alone and the wing alone are considered, and finally, the wing and body in combination are considered.

#### PRIMARY SYMBOLS

$A$	wing aspect ratio
$A_n, B_n$	strengths of axial multipoles according to linearized theory
$b$	wing span
$C_p$	pressure coefficient, local pressure minus free-stream static pressure divided by free-stream dynamic pressure
$c$	local wing chord
$c_j$	reference chord near wing-body junction (chord through the point of intersection of body and wing leading edge)
$c_R$	chord at wing center line
$c_T$	chord at wing tip
$\frac{E}{U_\infty}$	source strength
$f$	body fineness ratio (body length divided by maximum body diameter)
$K_n$	multipole strength parameter (see eq. (34))

$K_A$	plan-form convergence factor, $\frac{c_R - c_T}{b/2}$
$l$	body length (distance from nose to theoretical point of closure)
$L$	lateral distance to extended wing vertex for $\beta = 1$ (see sketch (1))
$M_\infty$	free-stream Mach number
$N$	see sketches (e), (f), and (m)
$N_1, N_2$	see sketch (c)
$r$	polar coordinate in $yz$ plane
$R$	body radius
$R_a$	body radius at wing leading edge
$\tilde{R}$	radius of equivalent circular body having equal cross-sectional area
$\Delta R$	incremental distortion of body shape from the circular shape having equal cross-sectional area
$S_b$	cross-sectional area of body
$\frac{t}{c}$	wing thickness to chord ratio
$U_\infty$	free-stream velocity
$\left. \begin{matrix} U, V, W \\ v_{(x)}, v_{(\theta)}, v_{(r)} \end{matrix} \right\}$	total velocities
$\left. \begin{matrix} u, v, w \\ v_{(x)}, v_{(y)}, v_{(z)} \end{matrix} \right\}$	perturbation velocities normalized by division by the free-stream velocity
$v_{(r)}$	radial component of perturbation velocity in $yz$ plane
$v_{(t)}, v_{(n)}$	tangential and normal perturbation velocities for an oblique source filament (see sketch (f))

$v(\theta)$	azimuthal component of perturbation velocity in yz plane
$v(r)_w$	radial perturbation velocity at body surface induced by wing sources
$\Delta v(r)_w$	$v(r)_w - \left[ v(r)_w \right]_{av}$
$\bar{x}_1$	$x - \bar{x}$
$x, y, z$	Cartesian coordinates
$z$	wing profile ordinate
$z', \frac{dz}{dx}$	airfoil slope in streamwise direction
$z'_m$	modified airfoil slope (see eq. (59))
$\xi, \eta, \zeta$	Cartesian coordinates normalized by division by a reference chord
$\xi_j$	Cartesian coordinate measured from the leading edge of the reference chord $c_j$ (see sketch (o))
$\bar{\xi}$	variable of integration (see sketches (g) and (l))
$\bar{\xi}^*$	$\xi - \beta \eta \tan \Lambda_e$
$\beta$	$\sqrt{ M^2 - 1 }$
$\beta_\Lambda$	$\sqrt{\sin^2 \Lambda + \beta^2 \cos^2 \Lambda} = \sqrt{1 - M^2 \cos^2 \Lambda}$
$\gamma$	ratio of specific heats (for air $\gamma = 1.4$ )
$\theta$	polar angle in yz plane
$\lambda$	wing plan-form taper ratio, $\frac{c_T}{c_R}$
$\phi$	perturbation potential
$\Lambda$	angle of sweep, positive when swept back
$\Lambda_e$	effective angle of sweep according to the Gthert compressibility rule

$(\quad)$	variable of integration
$(\quad)'$	first derivative with respect to the free-stream direction
$(\quad)''$	second derivative with respect to the free-stream direction
$f_n, g_n, h_n$	multipole influence functions (see eqs. (28) to (30))

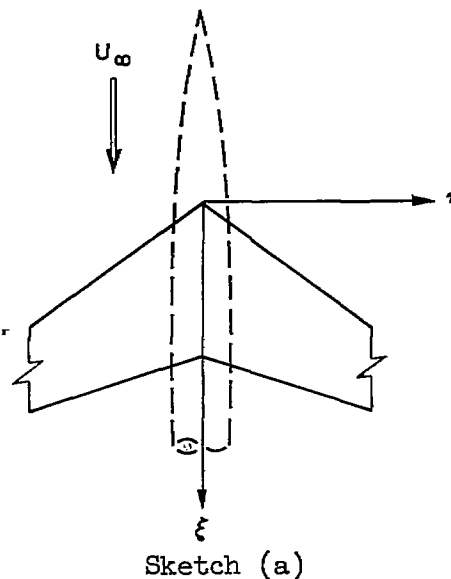
### Subscripts

av	average
b	body
e	equivalent configuration of the Göthert compressibility rule
j	condition along wing-body junction
LE	wing leading edge
TE	wing trailing edge
n	order of multipole
w	wing
$x, y, z, \theta$	partial derivatives when not enclosed by parentheses

## GENERAL THEORY

### Statement of the Problem

In this paper methods are presented for determining the subsonic flow about nonlifting wing-body combinations. These methods are based on the usual assumptions of linearized flow theory. The flow over the wing is to be determined by representing the nonlifting wing by a suitable distribution of planar sources. The wing is assumed to extend through the body as indicated in sketch (a).



It is further assumed that the wing-body combinations possess both lateral and vertical symmetry. The required boundary condition for tangential flow at the body surface is to be satisfied by placing along the body axis (which is coincident with the wind direction) suitable axial distributions of sources and multipoles.

Boundary Conditions for Tangential Flow  
at the Wing or Body Surface

If  $F(x,y,z) = 0$  is the general equation determining a body or wing shape in Cartesian coordinates, the boundary condition for tangential flow at the surface is

$$U \frac{\partial F}{\partial x} + V \frac{\partial F}{\partial y} + W \frac{\partial F}{\partial z} = 0 \quad (1)$$

In cylindrical coordinates the boundary condition can be written as

$$V(x) \frac{\partial F}{\partial x} + V(r) \frac{\partial F}{\partial R} + \frac{V(\theta)}{R} \frac{\partial F}{\partial \theta} = 0 \quad (2)$$

where  $F(x,R,\theta) = 0$  determines the body shape.

Wing theory. - If the ordinates for a thin airfoil are represented by the function  $Z = Z(x,y)$ , then

$$F(x,y,Z) = Z - Z(x,y) = 0$$

and the boundary condition at the surface is

$$U \frac{\partial Z}{\partial x} + V \frac{\partial Z}{\partial y} - W = 0 \quad (3)$$

For linearized, thin-airfoil theory, the second term can be neglected,  $U = U_\infty(1+u)$  is replaced by  $U_\infty$ ,

$$w = \frac{dZ}{dx} \quad z \rightarrow 0 \quad (4)$$

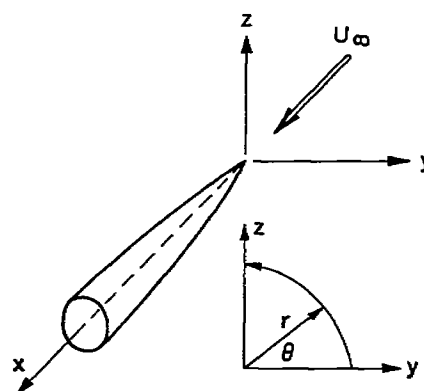
Body theory.— If the radii of a body, sketch (b), are represented by the function  $R = R(x, \theta)$ , the boundary condition at the body surface is

$$v_{(x)} \frac{\partial R}{\partial x} + \frac{v(\theta)}{R} \frac{\partial R}{\partial \theta} - v(r) = 0 \quad (5)$$

When the partial derivatives  $\partial R / \partial x$  and  $(\partial R / \partial \theta) / R$  are small,  $v_{(x)}$  is approximated

by  $U_\infty$  and the boundary condition in terms of perturbation velocities at the body surface is

$$\frac{\partial R}{\partial x} + \frac{v(\theta)}{R} \frac{\partial R}{\partial \theta} - v(r) = 0 \quad (6)$$



Sketch (b)

### Compressibility Corrections

The rules of correspondence between linearized compressible and incompressible flow in two dimensions were given originally by Prandtl. The extension of these rules to include flows in three dimensions was made by Göthert (ref. 7). The use of the Göthert rule is as follows: First, the lateral and vertical dimensions of the configuration are reduced by the factor  $\beta$  so as to obtain an "equivalent" configuration. The equivalent sweepback  $\Lambda_e$  of the wing reference line (or oblique source filament) is obtained from

$$\tan \Lambda_e = \frac{\tan \Lambda}{\beta} \quad (7)$$

Thus, the quantities  $\sin \Lambda$  and  $\cos \Lambda$  are replaced by

$$\left. \begin{aligned} \sin \Lambda_e &= \frac{\sin \Lambda}{\sqrt{\sin^2 \Lambda + \beta^2 \cos^2 \Lambda}} = \frac{\sin \Lambda}{\beta \Lambda} \\ \cos \Lambda_e &= \frac{\beta \cos \Lambda}{\sqrt{\sin^2 \Lambda + \beta^2 \cos^2 \Lambda}} = \frac{\beta \cos \Lambda}{\beta \Lambda} \end{aligned} \right\} \quad (8)$$



Next, the incompressible flow about the equivalent configuration is determined. Finally, the compressible flow is obtained from the calculated incompressible flow by increasing the velocity potential by the factor  $1/\beta^2$ , the axial-perturbation velocity is increased by the factor  $1/\beta^2$ , and the lateral and vertical velocities are increased by the factor  $1/\beta$  (the pressure coefficient is increased by the factor  $1/\beta^2$ ).

### Pressure Coefficient

The exact expression for the pressure coefficient (isentropic flow) is

$$C_p = \frac{2}{\gamma M_\infty^2} \left[ \left( 1 + \frac{\gamma-1}{2} M_\infty^2 \left\{ 1 - [(1+u)^2 + v^2 + w^2] \right\} \right)^{\frac{\gamma}{\gamma-1}} - 1 \right] \quad (9)$$

In order to obtain an approximation consistent with linearized theory this equation may be expanded to give (see, e.g., ref. 8)

$$C_p = -2u - (v^2 + w^2) + \beta^2 u^2 + M_\infty^2 u(v^2 + w^2) + \dots \quad (10)$$

For the linearized flow past planar systems, the first term is sufficient. For slender bodies it is necessary to consider additional terms and the appropriate expression is (in cylindrical coordinates)

$$C_p = -2u - \left[ v(r)^2 + v(\theta)^2 \right] \quad (11)$$

### Nonlifting Thin-Airfoil Theory

The basic linearized partial differential equation for subsonic flow is the well-known Prandtl-Glauert equation

$$(1 - M_\infty^2) \phi_{xx} + \phi_{yy} + \phi_{zz} = 0 \quad (12)$$

where  $M_\infty$  is the free-stream Mach number and  $\phi(x, y, z)$  is the perturbation potential.

Perturbation potential and velocities. - The perturbation potential subject to the boundary condition of equation (4) can be written in the form (see ref. 9 for the fundamentals of source-sink theory)

$$\phi(x, y, z) = \frac{-1}{4\pi\beta^2 U_\infty} \iint_{\Sigma} \frac{\beta E(\bar{x}, \beta \bar{y}) d\bar{x} d\bar{y}}{\sqrt{(x-\bar{x})^2 + \beta^2 [(y-\bar{y})^2 + z^2]}} \quad (13)$$

where the region of integration  $\Sigma$  extends over the entire plan form of the wing. This solution represents the potential due to a planar ( $z = 0$ ) distribution of sources having strength  $E$  per unit area.

The streamwise, lateral, and vertical perturbation velocities induced by the planar distribution of sources are:

$$u(x, y) = \frac{\partial \phi}{\partial x} = \frac{1}{4\pi\beta^2 U_\infty} \iint_{\Sigma} \frac{\beta (x-\bar{x}) E(\bar{x}, \beta \bar{y}) d\bar{x} d\bar{y}}{\left\{ (x-\bar{x})^2 + \beta^2 [(y-\bar{y})^2 + z^2] \right\}^{3/2}} \quad (14)$$

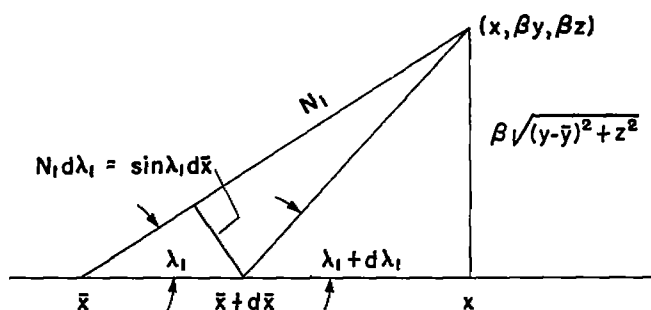
$$v(x, y) = \frac{\partial \phi}{\partial y} = \frac{1}{4\pi\beta U_\infty} \iint_{\Sigma} \frac{\beta^2 (y-\bar{y}) E(\bar{x}, \beta \bar{y}) d\bar{x} d\bar{y}}{\left\{ (x-\bar{x})^2 + \beta^2 [(y-\bar{y})^2 + z^2] \right\}^{3/2}} \quad (15)$$

$$w(x, y) = \frac{\partial \phi}{\partial z} = \frac{1}{4\pi\beta U_\infty} \iint_{\Sigma} \frac{\beta^2 z E(\bar{x}, \beta \bar{y}) d\bar{x} d\bar{y}}{\left\{ (x-\bar{x})^2 + \beta^2 [(y-\bar{y})^2 + z^2] \right\}^{3/2}} \quad (16)$$

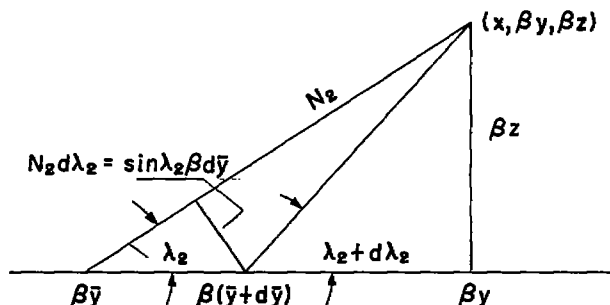
Determination of the source strength distribution. - An approximation for the source strength  $E$  can be obtained by finding a boundary value for  $w(x, y)$  as  $z \rightarrow 0$  and using that result in conjunction with the boundary condition of equation (4).

The boundary value for  $w$  as  $z \rightarrow 0+$  is to be obtained from

$$w_{z=0+} = \lim_{z \rightarrow 0+} \frac{1}{4\pi\beta U_\infty} \iint_{\Sigma} \frac{\beta^2 z E(\bar{x}, \beta \bar{y}) d\bar{x} d\bar{y}}{\left\{ (x-\bar{x})^2 + \beta^2 [(y-\bar{y})^2 + z^2] \right\}^{3/2}}$$



The above integrand is zero everywhere for  $z = 0$  except at the point  $x = \bar{x}$ ,  $y = \bar{y}$  where a singularity of the kind  $0/0$  occurs; consequently  $E(\bar{x}, \bar{y})$  may be replaced by  $E(x, y)$  and removed from under the integral signs. In order to evaluate this equation it is convenient to make the following changes of variables (see sketch (c)):



$$\lambda_1 = \sin^{-1} \frac{\beta \sqrt{(y-\bar{y})^2 + z^2}}{N_1}$$

$$\lambda_2 = \sin^{-1} \frac{\beta z}{N_2}$$

Sketch (c)

where

$$N_1 = \sqrt{(x-\bar{x})^2 + \beta^2 [(y-\bar{y})^2 + z^2]} = \frac{\beta \sqrt{(y-\bar{y})^2 + z^2}}{\sin \lambda_1}$$

$$N_2 = \beta \sqrt{(y-\bar{y})^2 + z^2} = \frac{\beta z}{\sin \lambda_2}$$

Finally there is obtained,

$$\begin{aligned} w_{z=0+} &= \frac{E(x, \beta y)}{4\pi\beta U_\infty} \int_0^\pi d\lambda_2 \int_0^\pi \sin \lambda_1 d\lambda_1 \\ &= \frac{E(x, \beta y)}{2\beta U_\infty} \end{aligned}$$

This result is subject to the boundary condition (4) and hence the source strength is defined as

$$\frac{E(x, \beta y)}{U_\infty} = 2\beta \frac{dz_u(x, \beta y)}{dx} \quad (17)$$

where  $dz_u/dx$  is the airfoil slope measured streamwise along the upper surface of the wing.

Source filaments.- In many cases, where the wing plan-form edges are straight-line elements, the use of source filaments in the mathematical representation of the flow is advantageous. In this way the determination of the perturbation potential is reduced from a two-dimensional integration over the entire plan form to a single integration performed in the streamwise direction. Details concerning the use of source filaments will be presented later in this report.

#### The General Solution in Cylindrical Coordinates for a Line of Axially Distributed Singularities

The linearized potential equation in cylindrical coordinates is

$$(1-M_\infty^2)\varphi_{xx} + \varphi_{rr} + \frac{1}{r}\varphi_r + \frac{1}{r^2}\varphi_{\theta\theta} = 0 \quad (18)$$

The linearized spatial flow about bodies or wing-body combinations requires a consideration of suitable distributions of sources and multipoles along the body axis with the axis of the multipoles aligned with the wind axis. The general solution of equation (18) consists of an infinite set of basic singularities referred to as multipoles (ref. 9, p. 527).

Perturbation potential and velocities.- The perturbation velocity potential of a line of axially distributed multipoles of order  $n$  in compressible flow is

$$\varphi(x, r, \theta) = \frac{-1}{4\pi\beta^2} \sum_n \left\{ (\beta r)^n \cos n\theta \int_0^l \frac{A_n(\bar{x}) d\bar{x}}{[(x-\bar{x})^2 + (\beta r)^2]^{n+(1/2)}} + \right. \\ \left. (\beta r)^n \sin n\theta \int_0^l \frac{B_n(\bar{x}) d\bar{x}}{[(x-\bar{x})^2 + (\beta r)^2]^{n+(1/2)}} \right\} \quad (19)$$

where  $A_n(x)$  and  $B_n(x)$  represent multipole strengths.

The perturbation velocity components can be obtained from equation (19) by partial differentiation in the axial, radial, and azimuthal directions. If it is assumed that  $A_n(0) = A_n(l) = 0$  and  $B_n(0) = B_n(l) = 0$ , the velocity components are:

$$u(x, r, \theta) = \frac{1}{4\pi\beta^2} \sum_n (2n+1)(\beta r)^n \int_0^l \frac{(x-\bar{x})[A_n(\bar{x})\cos n\theta + B_n(\bar{x})\sin n\theta]}{[(x-\bar{x})^2 + (\beta r)^2]^{n+(3/2)}} d\bar{x} \quad (20)$$

$$v(r)(x, r, \theta) = \frac{-1}{4\pi\beta} \sum_n n(\beta r)^{n-1} \int_0^l \frac{[A_n(\bar{x})\cos n\theta + B_n(\bar{x})\sin n\theta]}{[(x-\bar{x})^2 + (\beta r)^2]^{n+(1/2)}} d\bar{x} +$$

$$\frac{1}{4\pi\beta} \sum_n (2n+1)(\beta r)^{n+1} \int_0^l \frac{[A_n(\bar{x})\cos n\theta + B_n(\bar{x})\sin n\theta]}{[(x-\bar{x})^2 + (\beta r)^2]^{n+(3/2)}} d\bar{x} \quad (21)$$

$$v(\theta)(x, r, \theta) = \frac{1}{4\pi\beta} \sum_n n(\beta r)^{n-1} \int_0^l \frac{[A_n(\bar{x})\sin n\theta - B_n(\bar{x})\cos n\theta]}{[(x-\bar{x})^2 + (\beta r)^2]^{n+(1/2)}} d\bar{x} \quad (22)$$

If the change of variable

$$\bar{\delta} = \frac{\bar{x} - x}{\beta r} \quad (23)$$

is made, the above equations can be written in the following forms

$$\varphi(x, r, \theta) = \frac{-1}{4\pi\beta^2} \sum_n \frac{1}{(\beta r)^n} \int_{\frac{-x}{\beta r}}^{\frac{l-x}{\beta r}} [A_n(x + \beta r \bar{\delta})\cos n\theta +$$

$$B_n(x + \beta r \bar{\delta})\sin n\theta] f_n(\bar{\delta}) d\bar{\delta} \quad (24)$$

$$u(x, r, \theta) = \frac{-1}{4\pi\beta^2} \sum_n \frac{2n+1}{(\beta r)^{n+1}} \int_{\frac{-x}{\beta r}}^{\frac{l-x}{\beta r}} (A_n \cos n\theta + B_n \sin n\theta) g_n(\bar{\delta}) d\bar{\delta} \quad (25)$$

$$v_{(r)}(x, r, \theta) = \frac{1}{4\pi\beta} \sum_n \frac{1}{(\beta r)^{n+1}} \int_{\frac{-x}{\beta r}}^{\frac{l-x}{\beta r}} (A_n \cos n\theta + B_n \sin n\theta) [(2n+1)h_n(\bar{\delta}) - n f_n(\bar{\delta})] d\bar{\delta} \quad (26)$$

$$v_{(\theta)}(x, r, \theta) = \frac{1}{4\pi\beta} \sum_n \frac{n}{(\beta r)^{n+1}} \int_{\frac{-x}{\beta r}}^{\frac{l-x}{\beta r}} (A_n \sin n\theta - B_n \cos n\theta) f_n(\bar{\delta}) d\bar{\delta} \quad (27)$$

where

$$f_n(\bar{\delta}) = \frac{1}{(\bar{\delta}^2 + 1)^{n+(1/2)}} \quad (28)$$

$$g_n(\bar{\delta}) = \frac{\bar{\delta}}{(\bar{\delta}^2 + 1)^{n+(3/2)}} \quad (29)$$

$$h_n(\bar{\delta}) = \frac{1}{(\bar{\delta}^2 + 1)^{n+(3/2)}} \quad (30)$$

The variations of the influence functions  $f_n(\bar{\delta})$ ,  $g_n(\bar{\delta})$ , and  $h_n(\bar{\delta})$  with  $\bar{\delta}$  are shown in figure 1 for values of  $n$  equal to 0, 1, and 2.

An alternative expression for the axial perturbation velocity involving the influence function  $f_n(\bar{\delta})$  is obtained from equation (25) by integrating once by parts

$$u(x, r, \theta) = \frac{-1}{4\pi\beta^2} \sum_n \frac{1}{(\beta r)^{n+1}} \int_{\frac{-x}{\beta r}}^{\frac{l-x}{\beta r}} (A_n' \cos n\theta + B_n' \sin n\theta) f_n(\bar{\delta}) d\bar{\delta} \quad (31)$$

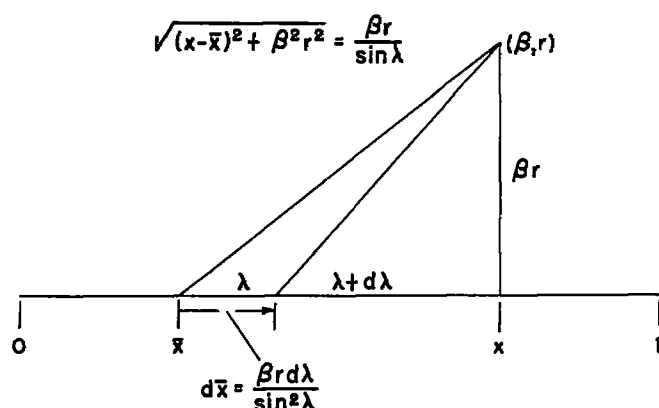
where

$$A_n' = \beta r \frac{dA_n(x+\beta r\delta)}{d\bar{x}}$$

$$B_n' = \beta r \frac{dB_n(x+\beta r\delta)}{d\bar{x}}$$

In the preceding results, the solution for an axial distribution of sources results when  $n$  is set equal to zero. For  $n = 1$  the "dipole" solution appears; for  $n = 2$ , the "quadripole" solution; etc. For small values of  $\beta r$  the attenuation of the induced perturbation velocities with increasing radial distance  $\beta r$  varies approximately as  $1/(\beta r)^{n+1}$ .

Limiting values for  $v(r)$  and  $v(\theta)$  as  $\beta r \rightarrow 0$ . - The direct use of the preceding equations in boundary-value problems is difficult since the unknown multipole strength functions must be related to the boundary condition (6). An approximation for the strength functions in terms of boundary values can be obtained by first investigating the limiting values for  $v(r)$  and  $v(\theta)$  as  $\beta r \rightarrow 0$ . The following change of variable is made (see sketch (d)),



Sketch (d)

$$\lambda = \sin^{-1} \frac{\beta r}{\sqrt{(x-\bar{x})^2 + \beta^2 r^2}}$$

As  $\beta r \rightarrow 0$  it is permissible to replace  $A_n(\bar{x})$  and  $B_n(\bar{x})$  by  $A_n(x)$  and  $B_n(x)$ . Consequently there are obtained the following limiting values for  $v(r)$  and  $v(\theta)$  as  $\beta r \rightarrow 0$ :

$$v(r) = \sum_{n=0}^{\infty} v(r)_n = \sum_{n=0}^{\infty} \frac{K_n}{4\pi\beta(\beta r)^{n+1}} [A_n(x)\cos n\theta + B_n(x)\sin n\theta] \quad (32)$$

$$v(\theta) = \sum_{n=0}^n v(\theta)_n = \sum_{n=0}^n \frac{K_n}{4\pi\beta(\beta r)^{n+1}} [A_n(x)\sin n\theta - B_n(x)\cos n\theta] \quad (33)$$

where

$$\left. \begin{aligned} K_0 &= K_1 = 2 \\ K_n &= \frac{(2)(4) \dots (2n)}{(1)(3) \dots (2n-1)} \end{aligned} \right\} \quad (34)$$

Equations (32) and (33) will be used with appropriate boundary conditions in subsequent sections of this report in order to determine multipole strength distributions for slender bodies or wing-body combinations.

#### The Munk-Jones Slender-Body Theory

It might be well to point out here the essential differences between linearized theory as used in this paper and the "slender-body" theory initiated by Munk and R. T. Jones (refs. 1 and 2). In the Munk-Jones theory, which has been applied and extended by numerous authors (see, in particular, refs. 3 to 6), the first term of the Prandtl-Glauert equation (12) is neglected in comparison with the second and third. The rate of change of the streamwise perturbation velocity is considered to be small in comparison with the rate of change of the vertical and lateral perturbation velocities. The application of slender-body theory involves solutions which satisfy Laplace's equation in planes normal to the free-stream direction, and the streamwise coordinate enters only as a parameter introduced by the body or wing-body cross-sectional area. For an axial distribution of singularities the slender-body counterpart of equation (19) is:

$$4\pi\phi(x,r) = 2S_b'(x)\ln \frac{\beta r}{2} - S_b'(x)\ln[x(l-x)] - \int_0^l \frac{S_b'(\bar{x}) - S_b'(x)}{|x-\bar{x}|} d\bar{x} +$$

$$\sum_{n=1}^{\infty} \left[ \frac{a_n(x)\cos n\theta}{r^n} + \frac{b_n(x)\sin n\theta}{r^n} \right]$$



where  $S_b'$  is the first derivative of the body cross-sectional area and the parameters  $a_n(x)$  and  $b_n(x)$  represent the multipole strengths.

The above relationship is a valid approximation only in the near vicinity of the body. It should be noted that the slender-body potential for a multipole of order  $n = 1$  or greater depends only on the parameters  $a_n(x)$  or  $b_n(x)$  and does not involve a line integration as in linearized theory. The Mach number effect enters only through the first term.

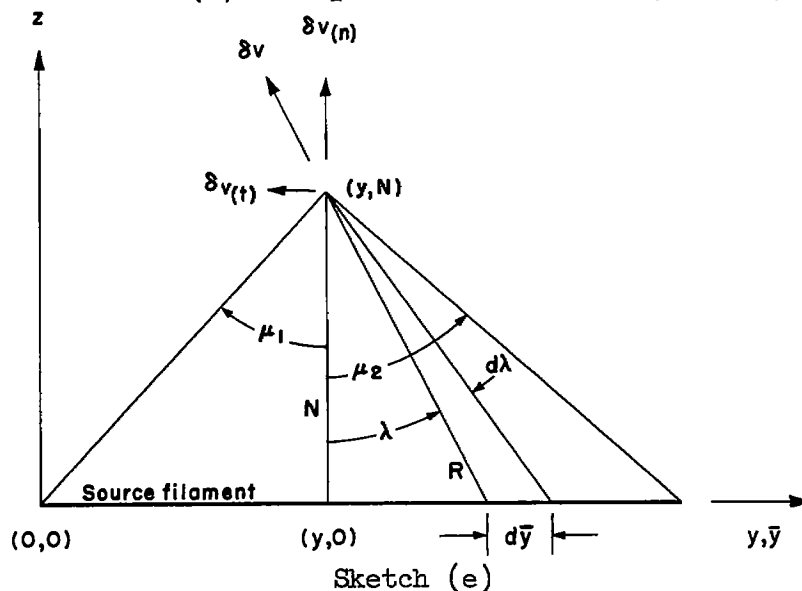
### THE NONLIFTING WING IN SUBSONIC FLOW

The nonlifting wing in subsonic flow may be represented by a suitable planar distribution of three-dimensional sources according to equation (13). If the wing leading and trailing edges are straight-line elements, and if the wing profile is geometrically similar at all spanwise stations, the evaluation of the flow over the wing can be best performed by a consideration of elementary source filaments. In this way, the double integration indicated by equation (13) is reduced to a single integration.

#### Untapered Wings

The flow about thin untapered wings has been studied in considerable detail (see, e.g., refs. 10 to 13). The following discussion presents certain additional considerations useful for numerical techniques.

The elementary source filament in incompressible flow.— Consider the source filament of constant strength  $E/U_\infty$  per unit length (incompressible flow) shown in sketch (e). The perturbation velocity  $\delta v$  (all velocity



components are normalized by division by the free-stream velocity) induced by the incremental source filament of length  $d\bar{y}$  at the point  $(y,N)$  is given by

$$\delta v = \frac{E \, d\bar{y}}{4\pi U_{\infty} R^2} = \frac{E \, d\lambda}{4\pi U_{\infty} N} \quad (35)$$

The tangential perturbation velocity induced by the entire source filament is given by

$$v_{(t)}(y, N) = - \int_{-\mu_1}^{\mu_2} \sin \lambda \, \delta v$$

$$= \frac{E}{4\pi U_{\infty} N} (\cos \mu_2 - \cos \mu_1) \quad (36)$$

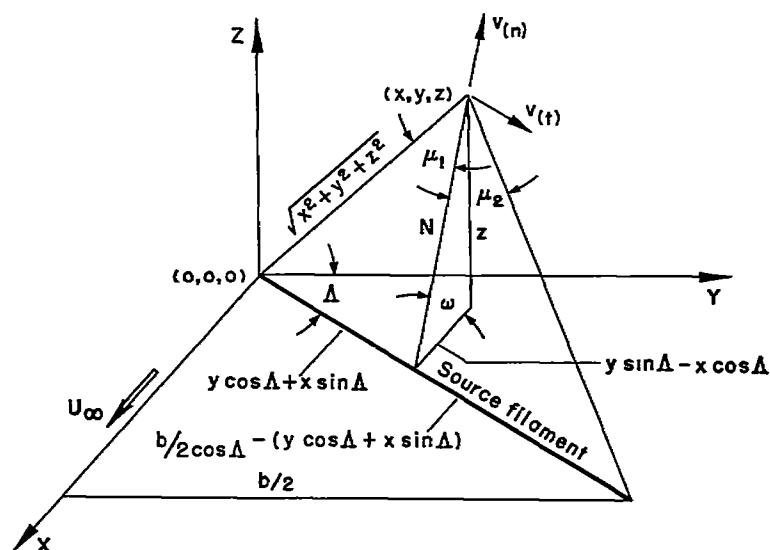
and the radial perturbation velocity is given by

$$v_{(n)}(y, N) = \int_{-\mu_1}^{\mu_2} \cos \lambda \, \delta v$$

$$= \frac{E}{4\pi U_{mN}} (\sin \mu_2 + \sin \mu_1) \quad (37)$$

Consider next the oblique source filament shown in sketch (f). The

$$N^2 = z^2 + (y \sin \Delta - x \cos \Delta)^2$$



Sketch (f)

normal and tangential velocity components induced at the point  $(x,y,z)$  are

$$v_{(n)}(x,y,z) = \frac{E}{4\pi U_{\infty} N} (\sin \mu_1 + \sin \mu_2) \quad (38)$$

$$v_{(t)}(x,y,z) = \frac{E}{4\pi U_{\infty} N} (\cos \mu_2 - \cos \mu_1) \quad (39)$$

The velocity components in the  $x,y,z$  directions are

$$v_{(x)} = v_{(t)} \sin \Lambda - v_{(n)} \cos \omega \cos \Lambda \quad (40)$$

$$v_{(y)} = v_{(t)} \cos \Lambda + v_{(n)} \cos \omega \sin \Lambda \quad (41)$$

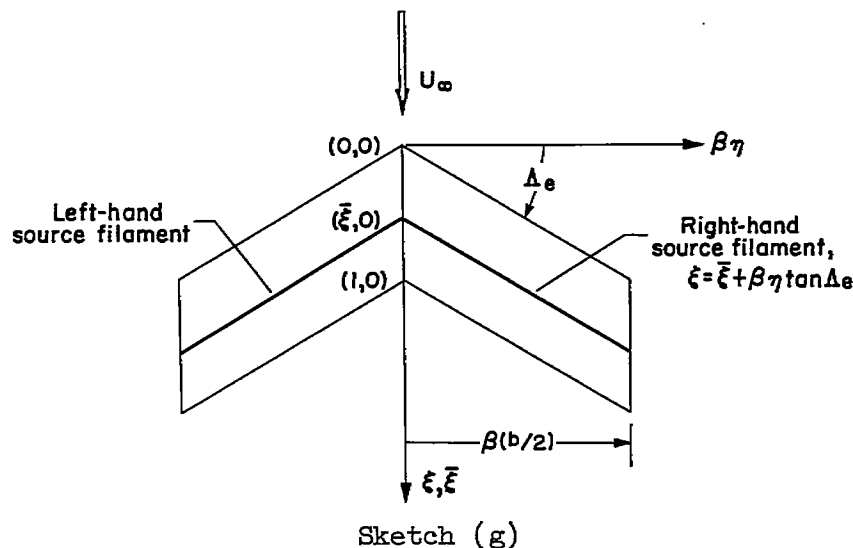
$$v_{(z)} = v_{(n)} \sin \omega \quad (42)$$

The sweptback wing. - The relationships given by equations (38) to (42) can be used to determine the compressible flow over thin, nonlifting, untapered wings if the Göthert rule is applied and if the source strength is defined as

$$\frac{E}{U_{\infty}} = 2 |\cos \Lambda_e| \beta Z' d\bar{x} \quad (43)$$

where  $Z'$  is the  $x$ -wise slope of the airfoil surface. Since only untapered wings are being considered here, the variable  $x$  is to be replaced by  $x - \bar{x}$  and an integration performed from  $\bar{x} = 0$  to  $\bar{x} = c$ . The factor  $\cos \Lambda_e$  appears in equation (43) since it is more convenient to perform the integration in the streamwise direction rather than in the direction normal to the oblique source filament. The absolute value signs are used in order that the source strength shall be properly defined for left-hand wing panels as well as for right-hand wing panels.

Consider the sweptback wing skown in sketch (g) where a coordinate system made dimensionless with respect to the root chord is used. The



axial, lateral, and vertical perturbation velocities for a compressible flow are to be obtained by evaluation of the following:

$$2\pi\beta^2 u(\xi, \eta, \zeta) = \begin{array}{c} \text{Right-hand wing} \\ |\cos \Lambda_e| \int_0^1 \beta Z' f(x) d\bar{\xi} + |\cos \Lambda_e| \int_0^1 \beta Z' f(x) d\bar{\xi} \end{array} \quad (44)$$

$$2\pi\beta v(\xi, \eta, \zeta) = \begin{array}{c} \text{Right-hand wing} \\ |\cos \Lambda_e| \int_0^1 \beta Z' f(y) d\bar{\xi} + |\cos \Lambda_e| \int_0^1 \beta Z' f(y) d\bar{\xi} \end{array} \quad (45)$$

$$2\pi\beta w(\xi, \eta, \zeta) = \begin{array}{c} \text{Right-hand wing} \\ |\cos \Lambda_e| \int_0^1 \beta Z' f(z) d\bar{\xi} + |\cos \Lambda_e| \int_0^1 \beta Z' f(z) d\bar{\xi} \end{array} \quad (46)$$

The first integrals on the right-hand side of equations (44) to (46) represent the source filaments on the right-hand wing panel and the second integrals those of the left-hand wing panel. The quantities  $f(x)$ ,  $f(y)$ ,  $f(z)$ , for the right-hand wing are:

$$f(x) = \left( \frac{\cos \mu_2 - \cos \mu_1}{N} \right) \sin \Lambda_e - \left( \frac{\sin \mu_1 + \sin \mu_2}{N} \right) \cos \omega \cos \Lambda_e \quad (47)$$

$$f(y) = \left( \frac{\cos \mu_2 - \cos \mu_1}{N} \right) \cos \Lambda_e + \left( \frac{\sin \mu_1 + \sin \mu_2}{N} \right) \cos \omega \sin \Lambda_e \quad (48)$$

$$f(z) = \left( \frac{\sin \mu_1 + \sin \mu_2}{N} \right) \sin \omega \quad (49)$$

Although these quantities can be expressed in algebraic terms with the help of sketch (f) and then substituted into the expressions for the velocity components (eqs. (44) to (46)), it is more convenient for numerical techniques to retain the identity of certain elementary quantities because of the extensive repetition involved in obtaining the final velocity components  $u$ ,  $v$ , and  $w$ . For the right-hand panel of a sweptback wing, the following are required:

$$\left. \begin{aligned} N &= \sqrt{(\beta \xi)^2 + R_2^2} \\ \omega &= \tan^{-1} \frac{\beta \xi}{R_2} \\ \mu_1 &= \tan^{-1} \frac{R_1}{N} \\ \mu_2 &= \tan^{-1} \left[ \frac{\frac{\beta(b/2)}{\cos \Lambda_e} - R_1}{N} \right] \end{aligned} \right\} \quad (50)$$

where

$$R_1 = \beta \eta \cos \Lambda_e + (\xi - \bar{\xi}) \sin \Lambda_e \quad (51)$$

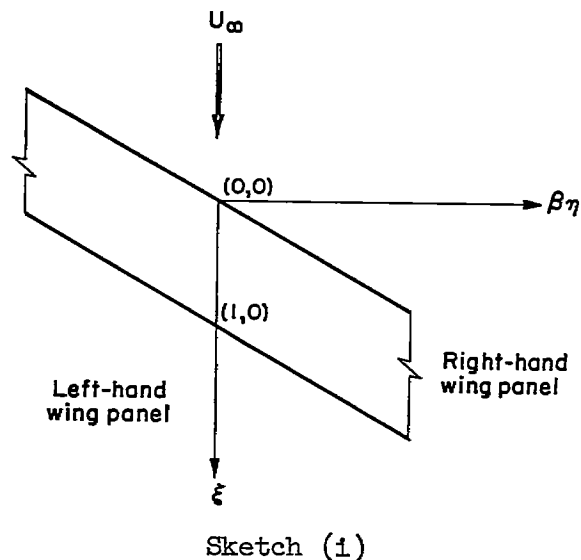
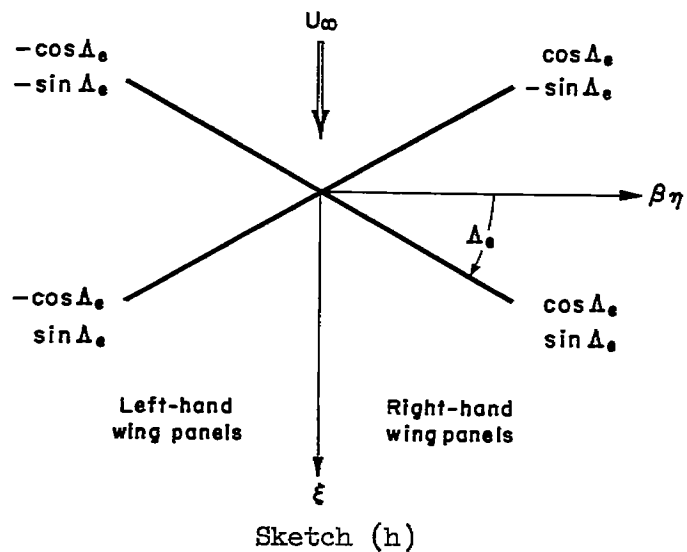
$$R_2 = \beta \eta \sin \Lambda_e - (\xi - \bar{\xi}) \cos \Lambda_e \quad (52)$$

(It should be noted that in the plane of the wing  $N$  reduces to  $N = |R_2|$  and  $\cos \omega = R_2/|R_2| = \text{sign } R_2$ .)

The relationships given by equations (50) to (52) were derived for a right-hand, sweptback wing panel. These results apply to other wing panels if the proper sign is affixed to  $\cos \Lambda_e$  and  $\sin \Lambda_e$  according to sketch (h). The distance  $\beta(b/2)$  is negative for left-hand wing panels.

The infinite oblique wing. - Formulas for the perturbation velocities induced by the infinite oblique wing can be obtained by use of the previous relationships if the infinite oblique wing is considered to be composed of two semi-infinite wing panels as shown in sketch (i).

For the left-hand wing panel,  $\mu_1 = \pi/2$ ,  $R_1 = -\beta\eta \cos \Lambda_e - (\xi - \bar{\xi}) \sin \Lambda_e$ , and  $R_2 = -\beta\eta \sin \Lambda_e + (\xi - \bar{\xi}) \cos \Lambda_e$ . For the right-hand wing panel,  $\mu_2 = \pi/2$ ,  $R_1 = \beta\eta \cos \Lambda_e + (\xi - \bar{\xi}) \sin \Lambda_e$ , and  $R_2 = \beta\eta \sin \Lambda_e - (\xi - \bar{\xi}) \cos \Lambda_e$ . The use of these definitions together with the definitions for  $N$ ,  $\mu_1$ , and  $\omega$  given in equation (50) lead to the following equations for perturbation velocities:



$$\beta^2 u(\xi, \eta, \zeta) = - \frac{\cos^2 \Lambda_e}{\pi} \int_0^1 \frac{[\beta\eta \sin \Lambda_e - (\xi - \bar{\xi}) \cos \Lambda_e] \beta Z' d\bar{\xi}}{(\beta\zeta)^2 + [\beta\eta \sin \Lambda_e - (\xi - \bar{\xi}) \cos \Lambda_e]^2}$$

$$\beta v(\xi, \eta, \zeta) = \beta \tan \Lambda_e u(\xi, \eta, \zeta)$$

$$\beta w(\xi, \eta, \zeta) = \frac{\cos \Lambda_e \beta \zeta}{\pi} \int_0^1 \frac{\beta Z' d\bar{\xi}}{(\beta\zeta)^2 + [\beta\eta \sin \Lambda_e - (\xi - \bar{\xi}) \cos \Lambda_e]^2}$$

Since the origin for  $\eta$  is immaterial for the infinite wing it is more convenient to write these equations for  $\eta = 0$ ,

$$\beta^2 u(\xi, \zeta) = - \frac{\cos \Lambda_e}{\pi} \int_0^1 \frac{(\bar{\xi} - \xi) \beta Z' d\bar{\xi}}{(\bar{\xi} - \xi)^2 + (\beta \zeta / \cos \Lambda_e)^2} \quad (53)$$

$$\beta v(\xi, \zeta) = \beta \tan \Lambda_e u(\xi, \zeta) \quad (54)$$

$$\beta w(\xi, \zeta) = \frac{\beta \zeta}{\pi \cos \Lambda_e} \int_0^1 \frac{\beta Z' d\bar{\xi}}{(\bar{\xi} - \xi)^2 + (\beta \zeta / \cos \Lambda_e)^2} \quad (55)$$

where  $\sin \Lambda_e$  and  $\cos \Lambda_e$  are defined by equation (8).

When the perturbation velocities are evaluated in the plane of the wing ( $\zeta = 0$ ), it is permissible to set  $\zeta = 0$  in equation (53) but not in equation (55). However, equation (55) reduces to  $w = Z'$  when evaluated in the plane of the wing.

If equation (53) is evaluated in the plane of the wing,

$$u(\xi, 0) = - \frac{\cos \Lambda}{\pi \beta_\Lambda} \int_0^1 \frac{Z' d\bar{\xi}}{\bar{\xi} - \xi} \quad (56)$$

it is seen that the pressure coefficient for thin-airfoil theory ( $C_p = -2u$ ) changes with Mach number according to the factor

$$\frac{1}{\beta_\Lambda} = \frac{1}{\sqrt{\sin^2 \Lambda + \beta^2 \cos^2 \Lambda}} = \frac{1}{\sqrt{1 - M^2 \cos^2 \Lambda}} \quad (57)$$

For the unswept wing this factor reduces to the Prandtl-Glauert factor  $1/\beta$ . The dependence of the compressibility effect on the Mach number component normal to the sweep line was pointed out by R. T. Jones, reference 14.

The leading-edge singularity for round-nose airfoils. - For round-nose airfoils the slope  $Z'$  is infinite at the nose and changes rapidly in value in the immediate vicinity of the nose. For numerical work it has been found convenient to replace the airfoil slope  $Z'$  by

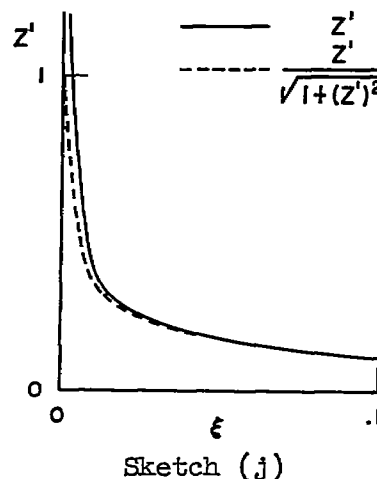
$$Z'_m = \frac{Z'}{\sqrt{1+(Z')^2}} \quad (58)$$

and the source strength (eq. (43)) by

$$\frac{E}{U_\infty} = 2 |\cos \Lambda_e| \beta Z'_m dx \quad (59)$$

This modification is illustrated in sketch (j) for an NACA 64A008 profile. The effect of this modification is to reduce somewhat the absolute values of the calculated perturbation velocities in the immediate vicinity fore and aft of the nose. In reference 15 it is suggested that the following correction (due to Riegel) be used,

$$U(x, Z) = \frac{U_L(x, 0)}{\sqrt{1+(Z')^2}}$$



where  $U$  is the total velocity over the airfoil, the subscript  $L$  refers to the linearized value. This is equivalent to

$$u = \frac{U_L}{\sqrt{1+(Z')^2}} + \frac{1 - \sqrt{1+(Z')^2}}{\sqrt{1+(Z')^2}}$$

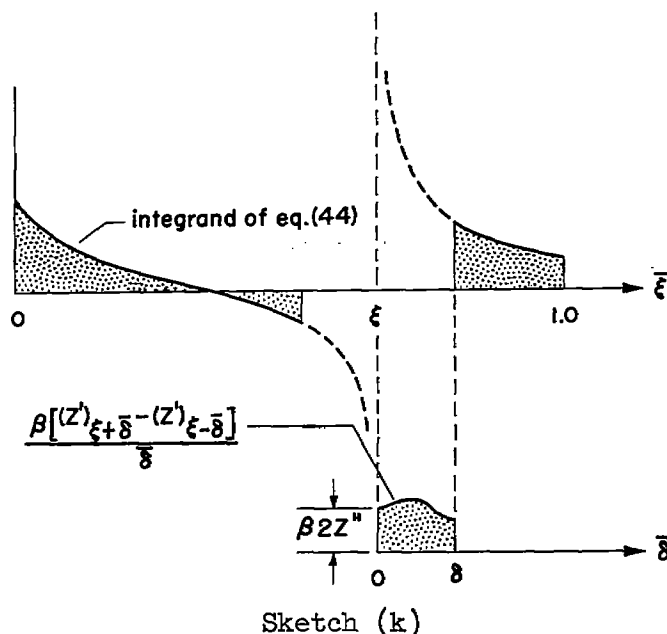
which has the limiting value  $u = -1$  at the nose. However, it is not possible to apply the Riegel rule at locations slightly forward of the airfoil nose.

The use of the modified airfoil slope  $Z'_m$  permits one to calculate reasonable and consistent perturbation velocities everywhere except at the wing leading and trailing edges where first-order theory gives infinite values except when the wing profile is cusped. For numerical work the calculated streamwise and lateral perturbation velocities in the plane of the wing have been terminated with values  $-\cos^2 \Lambda$  and  $\cos \Lambda \sin \Lambda$ , respectively, at the wing leading and trailing edges. The pressure coefficient may be estimated by substitution of the values  $u = -\cos^2 \Lambda$  and  $v = \cos \Lambda \sin \Lambda$  into equation (9).



The inherent singularity at  $\xi = 0$  as  $N \rightarrow 0$ . - If a numerical technique is used, the inherent singularity for  $\xi = 0$  at  $N \rightarrow 0$  can be circumvented in the following manner. For the infinite oblique wing the singularity at  $\xi = 0$  as  $\bar{\xi} \rightarrow \xi$  is avoided by writing equation (53) in the form

$$\beta^2 u(\xi, 0) = -\frac{\cos \Lambda_e}{\pi} \left[ \int_0^{\xi-\delta} \frac{\beta Z' d\bar{\xi}}{\bar{\xi}-\xi} + \int_0^{\delta} \frac{(\beta Z')_{\xi+\delta} - (\beta Z')_{\xi-\delta}}{\delta} d\bar{\xi} + \int_{\xi+\delta}^1 \frac{\beta Z'}{\bar{\xi}-\xi} d\bar{\xi} \right] \quad (60)$$



where  $\delta$  is any convenient subinterval bracketing the singular point, see sketch (k). The integrand of the second integral of equation (60) has the following finite value at the singular point

$$\lim_{\delta \rightarrow 0} \left[ \frac{(\beta Z')_{\xi+\delta} - (\beta Z')_{\xi-\delta}}{\delta} \right] = 2\beta Z''(\xi)$$

where  $Z''(\xi)$  is the second derivative of the airfoil ordinate evaluated at the singular point.

For swept wings an inherent singularity in the plane of the wing occurs when  $\bar{\xi}$  has the value

$$\bar{\xi}^* = \xi - \beta \eta \tan \Lambda_e \quad (61)$$

The singular integrals of equations (44) and (45) for  $\xi = 0$  can be avoided by writing these integrals in the form

$$\begin{aligned}
|\cos \Lambda_e| \int_0^1 \beta Z' f(x) d\bar{\xi} &= |\cos \Lambda_e| \int_0^{\bar{\xi}^* - \delta} \beta Z' f(x) d\bar{\xi} + |\cos \Lambda_e| \int_{\bar{\xi}^* + \delta}^1 \beta Z' f(x) d\bar{\xi} + \\
&\quad |\cos \Lambda_e| \int_0^{\delta} \left\{ \left[ \beta Z' f(x) \right]_{\bar{\xi}^* - \delta} + \left[ \beta Z' f(x) \right]_{\bar{\xi}^* + \delta} \right\} d\bar{\delta}
\end{aligned} \tag{62}$$

$$\begin{aligned}
|\cos \Lambda_e| \int_0^1 \beta Z' f(y) d\bar{\xi} &= |\cos \Lambda_e| \int_0^{\bar{\xi}^* - \delta} \beta Z' f(y) d\bar{\xi} + |\cos \Lambda_e| \int_{\bar{\xi}^* + \delta}^1 \beta Z' f(y) d\bar{\xi} + \\
&\quad |\cos \Lambda_e| \int_0^{\delta} \left\{ \left[ \beta Z' f(y) \right]_{\bar{\xi}^* - \delta} + \left[ \beta Z' f(y) \right]_{\bar{\xi}^* + \delta} \right\} d\bar{\delta}
\end{aligned} \tag{63}$$

where  $\delta$  is any convenient subinterval bracketing the singular point  $\bar{\xi} = \bar{\xi}^*$  (where  $\bar{\delta} = 0$ ). The integrands of the third integrals on the right-hand sides of equations (62) and (63) have the limiting values

$$2 \sin \Lambda_e \beta Z' \left[ \frac{1}{\frac{\beta(b/2)}{\cos \Lambda_e} - \frac{\beta \eta}{\cos \Lambda_e}} - \frac{1}{\frac{\beta \eta}{\cos \Lambda_e}} \right] - 4 \beta Z''$$

and

$$2 \cos \Lambda_e \beta Z' \left[ \frac{1}{\frac{\beta(b/2)}{\cos \Lambda_e} - \frac{\beta \eta}{\cos \Lambda_e}} - \frac{1}{\frac{\beta \eta}{\cos \Lambda_e}} \right] + 4 \tan \Lambda_e \beta Z''$$

respectively, at the singular point. (This technique for avoiding the singularity in the plane of the wing was illustrated previously for the infinite oblique wing in sketch (k).)

The distortion velocity at the center line of a sweptback wing.- At the center line of the sweptback wing a unique result is obtained whereby the streamwise velocity is found to be equal to that for the infinite oblique wing plus a distortion velocity of the Ackeret type (proportional to  $Z'$ ), see reference 11, 12, or 13. This result is easily obtained in the following manner. First consider the right-hand, sweptback wing panel. The streamwise perturbation velocity at the center line can be obtained by use of the relationships of equations (44) to (52) with  $\xi = 0$ ,  $u_2 = \pi/2$ ,  $N = |R_2|$ . There is obtained

$$2\pi\beta^2 u(\xi, 0, 0) = \lim_{\beta\eta \rightarrow 0} \left\{ -\cos^2 \Lambda_e \int_0^1 \frac{\beta Z' d\bar{\xi}}{\beta\eta \sin \Lambda_e - (\xi - \bar{\xi}) \cos \Lambda_e} - \right. \\ \left. \cos \Lambda_e \int_0^1 \frac{\beta\eta \beta Z' d\bar{\xi}}{[\beta\eta \sin \Lambda_e - (\xi - \bar{\xi}) \cos \Lambda_e] \sqrt{(\xi - \bar{\xi})^2 + (\beta\eta)^2}} \right\} \quad (64)$$

In the first integral  $\eta$  can be set equal to zero and the result is equal to one half that for the infinite oblique wing. The results for the left-hand, sweptback wing panel can be expressed in a form identical with equation (64). Thus, the distortion velocity at the wing center line, ( $\beta\eta = 0$ ),

$$u_d = u_{\text{center line}} - u_{\text{oblique wing}}$$

is given by

$$\beta^2 u_d(\xi) = \lim_{\beta\eta \rightarrow 0} \left\{ -\frac{\cos \Lambda_e}{\pi} \int_0^1 \frac{\beta\eta \beta Z' d\bar{\xi}}{[\beta\eta \sin \Lambda_e - (\xi - \bar{\xi}) \cos \Lambda_e] \sqrt{(\xi - \bar{\xi})^2 + (\beta\eta)^2}} \right\}$$

It is clear that the above integrand is zero everywhere for  $\beta\eta = 0$  except at the singular point where the integrand is  $0/0$ . In order to obtain the limit, an integration is performed from  $\xi - \beta\eta \tan \Lambda_e - \delta$  to  $\xi - \beta\eta \tan \Lambda_e - \epsilon$  and from  $\xi - \beta\eta \tan \Lambda_e + \epsilon$  to  $\xi - \beta\eta \tan \Lambda_e + \delta$  with  $\beta Z'(\xi)$  replaced by  $\beta Z'(\xi) + \beta Z''(\xi)\bar{\xi}$ . The Cauchy principal value is obtained by letting  $\epsilon \rightarrow 0$  and the final result is independent of  $\delta$ ,

$$u_d(\xi) = - \frac{\cos \Lambda_e Z'(\xi)}{\pi \beta} \ln \frac{1 + \sin \Lambda_e}{1 - \sin \Lambda_e} \quad (65)$$

It should be pointed out here that, in the original body contouring method of Küchemann (ref. 13), the distortion velocity at the wing-body juncture is assumed to be that given by equation (65).

For sweptback wings of finite aspect ratio the perturbation velocity at the center line for  $\xi = 0$  is

$$u = u_{\text{oblique wing}} + u_d + \frac{|\cos \Lambda_e|}{\pi \beta^2} \int_0^1 \left( \frac{\sin \Lambda_e}{\sqrt{R_2^2 + \left[ \frac{\beta(b/2)}{\cos \Lambda_e} - R_1 \right]^2}} + \frac{\cos \Lambda_e}{R_2} \left\{ 1 - \frac{\frac{\beta(b/2)}{\cos \Lambda_e} - R_1}{\sqrt{R_2^2 + \left[ \frac{\beta(b/2)}{\cos \Lambda_e} - R_1 \right]^2}} \right\} \right) \beta Z' d\bar{\xi}$$

where  $R_1 = (\xi - \bar{\xi}) \sin \Lambda_e$  and  $R_2 = (\bar{\xi} - \xi) \cos \Lambda_e$ . (The above integral is not singular at the singular point  $\bar{\xi} = \xi^*$ .)

In the immediate vicinity of the tip of a sweptback wing the streamwise perturbation velocity may be approximated by the following:

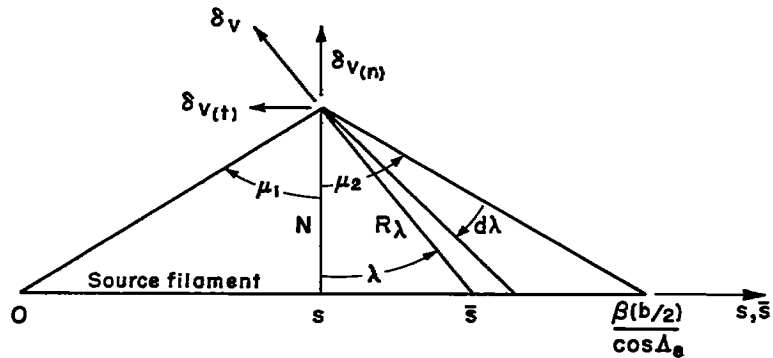
$$u = u_{\text{oblique wing}} - \frac{u_d}{2}$$

#### Wings Having Tapered Plan Forms

The thin, nonlifting wing with tapered plan form has been considered in references 16 and 17 where an evaluation of equations (14) to (16) was performed by integration in the streamwise direction first, and numerical results could be obtained only by laborious expansions into infinite series. However, as will be shown by the following analysis, it is possible to compute the flow about the tapered wing by use of the source filament concept in a manner similar to that for the untapered wing.



per unit length of  $\bar{s}$ , see sketch (m). The perturbation velocity components induced by this source filament in directions normal and tangential to the filament are



Sketch (m)

$$\begin{aligned}
 v_{(n)} &= \int_{-\mu_1}^{\mu_2} \cos \lambda \delta v \\
 &= \frac{\beta Z'}{2\pi} \left[ \left( \frac{\beta L}{\sin \sigma} - R_1 \right) (\sin \mu_2 + \sin \mu_1) + (\cos \mu_2 - \cos \mu_1) \right] d\sigma \quad (66)
 \end{aligned}$$

$$\begin{aligned}
 v_{(t)} &= - \int_{-\mu_1}^{\mu_2} \sin \lambda \delta v \\
 &= \frac{\beta Z'}{2\pi} \left\{ \left( \frac{\beta L}{\sin \sigma} - R_1 \right) (\cos \mu_2 - \cos \mu_1) - (\sin \mu_2 + \sin \mu_1) + \right. \\
 &\quad \left. \log \left[ \tan \left( \frac{\pi}{4} + \frac{\mu_2}{2} \right) \tan \left( \frac{\pi}{4} + \frac{\mu_1}{2} \right) \right] \right\} d\sigma \quad (67)
 \end{aligned}$$

and the streamwise, lateral, and vertical velocity components induced by the filament are given by equations (40) to (42). The quantities  $N$ ,  $R_1$ ,  $R_2$ ,  $\omega$ ,  $\mu_1$ , and  $\mu_2$  are the same quantities defined previously by equations (50) to (52). The parameter  $\bar{\xi}$ , see sketch (l), is related to the angle  $\sigma$  by the following relationship

$$\sigma = \cot^{-1} \left( \cot \sigma_{LE} - \frac{\bar{\xi}}{\beta L} \right) \quad (68)$$

For numerical work it is convenient to use the parameter  $\bar{\xi}$  as the variable of integration; hence,  $d\sigma$  in equations (66) and (67) is to be replaced by

$$d\sigma = \frac{d\sigma}{d\bar{\xi}} d\bar{\xi} = \frac{|\cos \Lambda_e|}{\beta L / \cos \Lambda_e} d\bar{\xi} \quad (69)$$

The sweptback wing.— The perturbation velocities induced by the right-hand wing panel shown in sketch (1) are obtained by evaluation of the following:

$$2\pi\beta^2 u = \int_0^1 |\cos \Lambda_e| \beta Z' \left[ g(x) + h(x) \right] d\bar{\xi} \quad (70)$$

$$2\pi\beta v = \int_0^1 |\cos \Lambda_e| \beta Z' \left[ g(y) + h(y) \right] d\bar{\xi} \quad (71)$$

$$2\pi\beta w = \int_0^1 |\cos \Lambda_e| \beta Z' \left[ g(z) + h(z) \right] d\bar{\xi} \quad (72)$$

where

$$g(x) = \left( 1 - \frac{R_1}{\beta L / \cos \Lambda_e} \right) \left[ \left( \frac{\cos \mu_2 - \cos \mu_1}{N} \right) \sin \Lambda_e - \left( \frac{\sin \mu_2 + \sin \mu_1}{N} \right) \cos \omega \cos \Lambda_e \right] \quad (73)$$

$$g(y) = \left( 1 - \frac{R_1}{\beta L / \cos \Lambda_e} \right) \left[ \left( \frac{\cos \mu_2 - \cos \mu_1}{N} \right) \cos \Lambda_e + \left( \frac{\sin \mu_2 + \sin \mu_1}{N} \right) \cos \omega \sin \Lambda_e \right] \quad (74)$$

$$g(z) = \left( 1 - \frac{R_1}{\beta L / \cos \Lambda_e} \right) \left( \frac{\sin \mu_2 + \sin \mu_1}{N} \right) \sin \omega \quad (75)$$

$$h(x) = \frac{1}{\beta L / \cos \Lambda_e} \left\{ \sin \Lambda_e \ln \left[ \left( \frac{1 + \sin \mu_1}{\cos \mu_1} \right) \left( \frac{1 + \sin \mu_2}{\cos \mu_2} \right) \right] - \right. \\ \left. (\sin \mu_2 + \sin \mu_1) \sin \Lambda_e - (\cos \mu_2 - \cos \mu_1) \cos \omega \cos \Lambda_e \right\} \quad (76)$$

$$h(y) = \frac{1}{\beta L / \cos \Lambda_e} \left\{ \cos \Lambda_e \ln \left[ \left( \frac{1 + \sin \mu_1}{\cos \mu_1} \right) \left( \frac{1 + \sin \mu_2}{\cos \mu_2} \right) \right] - \right. \\ \left. (\sin \mu_2 + \sin \mu_1) \cos \Lambda_e + (\cos \mu_2 - \cos \mu_1) \cos \omega \sin \Lambda_e \right\} \quad (77)$$

$$h(z) = \frac{1}{\beta L / \cos \Lambda_e} \left[ (\cos \mu_2 - \cos \mu_1) \sin \omega \right] \quad (78)$$

When the parameter  $\beta L / \cos \Lambda_e$  becomes infinitely large the  $h$  functions vanish and the  $g$  functions reduce to the relationships given previously for the untapered wing (eqs. (47) to (49)). If the plan-form convergence factor, defined as

$$\frac{K_A}{\beta} = \frac{C_R - C_T}{\beta(b/2)} \quad (79)$$

is small, say less than 0.5, the  $h$  functions may be neglected in equations (70) to (72).

Evaluation of the streamwise and lateral perturbation velocities in the plane of the wing.— If a numerical technique is used, the singularity in the plane of the wing at  $\xi^*$  (that is, at  $N = 0$ ) can be avoided by a procedure similar to that used for the untapered wing, with the exception that the log term appearing in  $h(x)$  and  $h(y)$  must be evaluated separately. For  $\xi = 0$  it is convenient to write equations (70) and (71) in the form



$$\begin{aligned}
2\pi\beta^2 u = & \int_0^{\bar{\xi}^*-\delta} |\cos \Lambda_e| \beta Z' \left[ g(x) + h(x) \right] d\bar{\xi} + \int_{\bar{\xi}^*+\delta}^1 |\cos \Lambda_e| \beta Z' \left[ g(x) + h(x) \right] d\bar{\xi} + \\
& \int_0^\delta |\cos \Lambda_e| \left\{ \left[ \beta Z' g(x) \right]_{\bar{\xi}^*+\delta} + \left[ \beta Z' g(x) \right]_{\bar{\xi}^*-\delta} \right\} d\bar{\xi} + \\
& \int_{\bar{\xi}^*-\delta}^{\bar{\xi}^*+\delta} |\cos \Lambda_e| \beta Z' h(x) d\bar{\xi} \quad (80)
\end{aligned}$$

$$\begin{aligned}
2\pi\beta v = & \int_0^{\bar{\xi}^*-\delta} |\cos \Lambda_e| \beta Z' \left[ g(y) + h(y) \right] d\bar{\xi} + \int_{\bar{\xi}^*+\delta}^1 |\cos \Lambda_e| \beta Z' \left[ g(y) + h(y) \right] d\bar{\xi} + \\
& \int_0^\delta |\cos \Lambda_e| \left\{ \left[ \beta Z' g(y) \right]_{\bar{\xi}^*+\delta} + \left[ \beta Z' g(y) \right]_{\bar{\xi}^*-\delta} \right\} d\bar{\xi} + \\
& \int_{\bar{\xi}^*-\delta}^{\bar{\xi}^*+\delta} |\cos \Lambda_e| \beta Z' h(y) d\bar{\xi} \quad (81)
\end{aligned}$$

where  $\delta$  is any small, convenient subinterval (say  $\delta = 0.05$ ) bracketing the singular point.

The first three integrals of equations (80) and (81) are not singular. The third integrals of equations (80) and (81) have the following limiting values, as  $\bar{\delta} \rightarrow 0$  for a right-hand wing panel,

$$2 \frac{\sin \Lambda_e \cos \Lambda_e \beta Z'}{\beta L / \cos \Lambda_e} \left( \frac{\beta L}{\cos \Lambda_e} - \frac{\beta \eta}{\cos \Lambda_e} \right) \left[ \frac{1}{\frac{\beta(b/2)}{\cos \Lambda_e} - \frac{\beta \eta}{\cos \Lambda_e}} - \frac{1}{\frac{\beta \eta}{\cos \Lambda_e}} \right] -$$

$$4 \frac{\beta L / \cos \Lambda_e}{\cos \Lambda_e} \frac{\partial \left( \frac{\cos^2 \Lambda_e \beta Z'}{\beta L / \cos \Lambda_e} \right)}{\partial \bar{\xi}}$$

and

$$2 \frac{\cos^2 \Lambda_e \beta Z'}{\beta L / \cos \Lambda_e} \left( \frac{\beta L}{\cos \Lambda_e} - \frac{\beta \eta}{\cos \Lambda_e} \right) \left[ \frac{1}{\frac{\beta(b/2)}{\cos \Lambda_e} - \frac{\beta \eta}{\cos \Lambda_e}} - \frac{1}{\frac{\beta \eta}{\cos \Lambda_e}} \right] +$$

$$4 \frac{\tan \Lambda_e (\beta L / \cos \Lambda_e)}{\cos \Lambda_e} \frac{\partial \left( \frac{\cos^2 \Lambda_e \beta Z'}{\beta L / \cos \Lambda_e} \right)}{\partial \bar{\xi}}$$

respectively, at the singular point. (The indicated partial derivatives may be evaluated graphically.)

The integrands of the fourth integrals of equations (80) and (81) are logarithmically singular at  $\bar{\xi} \rightarrow \bar{\xi}^*$  and do not change sign at the singular point  $\bar{\xi}^*$ . These integrals can be evaluated approximately if

$$\delta < \frac{\beta \eta / \cos \Lambda_e}{\sin \Lambda_e}, \quad \frac{\frac{\beta(b/2)}{\cos \Lambda_e} - \frac{\beta \eta}{\cos \Lambda_e}}{\sin \Lambda_e} \quad \text{as follows:}$$

$$\int_{\bar{\xi}^*-\delta}^{\bar{\xi}^*+\delta} \cos \Lambda_e \beta Z' h(x) d\bar{\xi}$$

$$\approx \frac{4\delta \sin \Lambda_e \cos \Lambda_e \beta Z'}{\beta L / \cos \Lambda_e} \ln \left\{ \frac{2 \sqrt{\frac{\beta \eta}{\cos \Lambda_e} \left[ \frac{\beta(b/2)}{\cos \Lambda_e} - \frac{\beta \eta}{\cos \Lambda_e} \right]}}{\left(1 - \frac{\beta \eta}{\beta L}\right) \delta \cos \Lambda_e} \right\}$$

$$\int_{\bar{\xi}^*-\delta}^{\bar{\xi}^*+\delta} \cos \Lambda_e \beta Z' h(y) d\bar{\xi}$$

$$\approx \frac{4\delta \cos^2 \Lambda_e \beta Z'}{\beta L / \cos \Lambda_e} \ln \left\{ \frac{2 \sqrt{\frac{\beta \eta}{\cos \Lambda_e} \left[ \frac{\beta(b/2)}{\cos \Lambda_e} - \frac{\beta \eta}{\cos \Lambda_e} \right]}}{\left(1 - \frac{\beta \eta}{\beta L}\right) \delta \cos \Lambda_e} \right\}$$

At the wing center line the lateral velocity is zero because of symmetry. For numerical work, the streamwise perturbation velocity cannot be obtained from equation (80) by setting  $\beta \eta = 0$  since the function  $g(x)$  contains an indeterminate form for  $\beta \eta = 0$ . However, equation (80) can be used at the wing center line if the quantity  $2\pi\beta^2 u_d$  is added to the right-hand side. At the wing center line the third integral of equation (80) has the following limiting value as  $\delta \rightarrow 0$ :

$$4 \cos \Lambda_e \left[ \frac{\sin \Lambda_e \beta Z'}{\beta(b/2)/\cos \Lambda_e} - \beta Z'' \right]$$

At the wing center line the fourth integral of equation (80) contributes the approximate value,

$$\frac{4\delta \sin \Lambda_e \cos \Lambda_e \beta Z'}{\beta L / \cos \Lambda_e} \ln \left[ \frac{2 \frac{\beta(b/2)}{\cos \Lambda_e}}{\delta \cos \Lambda_e} \right]$$

The above results for the right-hand, sweptback wing panel can be used for other wing panels if the signs of  $\cos \Lambda_e$  and  $\sin \Lambda_e$  are changed in accordance with the sign convention of sketch (h). The angle  $\sigma$ , which is the complement of the Göttert equivalent sweep angle  $\Lambda_e$ , is considered to be a positive angle (in the second quadrant) when measured counterclockwise as in sketch (i). For the left-hand sweptback wing panel, the angle  $\sigma$  is measured clockwise and hence is a negative angle (in the fourth quadrant). The distances  $\beta(b/2)$  and  $\beta L$  are considered to be negative for left-hand wing panels.

#### THE SUBSONIC FLOW ABOUT NONLIFTING BODIES

The linearized spatial flow about bodies can be represented by suitable axial distributions of sources and multipoles according to the general solution (19) where the body axis and the axes of the multipoles are aligned with the wind axis. It is assumed that the body cross-sectional area distribution terminates with zero first derivative,  $S'(0) = S'(l) = 0$ . It is further assumed that the function describing the body shape,  $R(x, \theta)$ , is single-valued in  $\theta$  and possesses smooth and continuous partial derivatives.

When equations (32) to (34) are used in conjunction with the boundary condition (6) there results the following general requirement to be satisfied in the evaluation of the strength distribution functions  $A_n$  and  $B_n$ :

$$\frac{\partial \beta R}{\partial x} + \sum_{n=0}^{\infty} \frac{K_n}{4\pi(\beta R)^{n+1}} [A_n(x) \sin n\theta - B_n(x) \cos n\theta] \frac{\partial \beta R}{\beta R \partial \theta} -$$

$$\sum_{n=0}^{\infty} \frac{K_n}{4\pi(\beta R)^{n+1}} [A_n(x) \cos n\theta + B_n(x) \sin n\theta] = 0 \quad (82)$$

### Axially Symmetric Bodies

For circular bodies, the source solution ( $n = 0$ ) is the only solution involved and the boundary condition (82) reduces to

$$A_0(x) = 2\pi\beta R \frac{\partial\beta R}{\partial x} = \beta^2 S'_b(x) \quad (83)$$

where  $S'_b(x)$  is the first derivative of the body cross-sectional area.

The perturbation-velocity components are

$$u(x,r) = \frac{1}{4\pi} \int_0^l \frac{(x-\bar{x})S'_b(\bar{x})}{[(x-\bar{x})^2 + \beta^2 r^2]^{3/2}} d\bar{x} \quad (84)$$

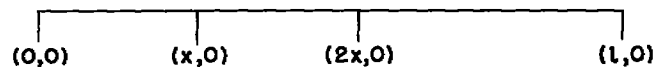
$$v_{(r)}(x,r) = \frac{\beta r}{4\pi} \int_0^l \frac{S'_b(\bar{x})}{[(x-\bar{x})^2 + \beta^2 r^2]^{3/2}} d\bar{x} \quad (85)$$

and the pressure coefficient is to be calculated from

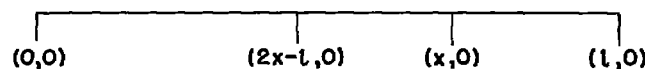
$$C_p = -2u - v_{(r)}^2$$

When the strength distribution of an axial source line cannot be expressed analytically, the integration of equations (84) and (85) must be performed by a suitable numerical means. Although the integrand is not singular at  $\bar{x} = 0$  for either equation, the integrand of equation (84) changes sign and varies greatly in magnitude near  $\bar{x} = x$  for small  $\beta r$ . Consequently, the numerical evaluation of equation (84) is simplified considerably if the region of integration is separated into subintervals (see sketch (n)) and this equation written in the form

$$x < l/2$$



$$x > l/2$$



Sketch (n)

$$u(x,r) = \frac{1}{4\pi} \int_0^{2x} \frac{\bar{\delta}_1}{[(\bar{\delta}_1)^2 + \beta^2 r^2]^{3/2}} \left[ S'_b(x-\bar{\delta}_1) - S'_b(x+\bar{\delta}_1) \right] d\bar{\delta}_1 + \left. \begin{aligned} & \frac{1}{4\pi} \int_{l-2x}^l \frac{(x-\bar{x}) S'_b(\bar{x})}{[(x-\bar{x})^2 + \beta^2 r^2]^{3/2}} d\bar{x} \\ & x < \frac{l}{2} \end{aligned} \right\} \quad (86)$$

$$u(x,r) = \frac{1}{4\pi} \int_0^{l-x} \frac{\bar{\delta}_1}{[(\bar{\delta}_1)^2 + \beta^2 r^2]^{3/2}} \left[ S'_b(x-\bar{\delta}_1) - S'_b(x+\bar{\delta}_1) \right] d\bar{\delta}_1 + \left. \begin{aligned} & \frac{1}{4\pi} \int_0^{2x-l} \frac{(x-\bar{x}) S'_b(\bar{x})}{[(x-\bar{x})^2 + \beta^2 r^2]^{3/2}} d\bar{x} \\ & x > \frac{l}{2} \end{aligned} \right\} \quad (87)$$

where  $\bar{\delta}_1 = x - \bar{x}$ .

#### Nonsymmetric Bodies

For the flow about bodies which do not possess axial symmetry, a consideration of both sources and multipoles is required. The body shape may be designated by

$$R(x, \theta) = \tilde{R}(x) + \sum_{n=1}^n \Delta R_n(x, \theta) \quad (88)$$

where  $\tilde{R}$  is the radius of a circular body having an identical axial distribution of cross-sectional area  $S_p(x)$  and where  $\Delta R_n$  is the incremental change in body radius associated with the  $n$ th order multipole distribution.

In most practical cases the body will possess vertical and lateral symmetry and will be nearly circular in cross section. In this case the boundary condition (82) can be simplified to the following,

$$\frac{\partial \beta R}{\partial x} - \frac{1}{4\pi} \sum_{n=0,2,4,\dots}^n \frac{K_n}{(\beta R)^{n+1}} A_n(x) \cos n\theta = 0 \quad (89)$$

In order to solve equation (89) for the strength functions  $A_n(x)$  it is convenient to express the body slope in the form (primes denote differentiation with respect to  $x$ ),

$$\beta R'(x, \theta) = \beta \tilde{R}'(x) + \sum_{n=2,4,6,\dots}^n \frac{\beta \Delta R'_n(x, \theta) (\beta R)^{n+1}}{(\beta R)^{n+1}} \quad (90)$$

It is assumed that the even function  $\beta \Delta R' = \beta (R' - \tilde{R}')$  can be represented by a Fourier cosine series and thus equation (90) becomes

$$\beta R'(x, \theta) = \beta \tilde{R}'(x) + \sum_{n=2,4,6,\dots}^n \frac{a_n(x) \cos n\theta}{(\beta R)^{n+1}} \quad (91)$$

where

$$a_n(x) = \frac{4}{\pi} \int_0^{\pi/2} \beta \Delta R' (\beta R)^{n+1} \cos n\theta \, d\theta \quad (92)$$

If the relationships (91) and (92) are substituted into (89) and if the coefficients of  $\cos n\theta$  are set equal to zero, there results in the following solutions for the source and multipole strengths:

$$\left. \begin{aligned} A_0 &= 2\pi\beta^2 \bar{R} \bar{R}' \\ A_n &= \frac{16}{K_n} \int_0^{\pi/2} \beta \Delta R' (\beta R)^{n+1} \cos n\theta \, d\theta \end{aligned} \right\} \quad (93)$$

where

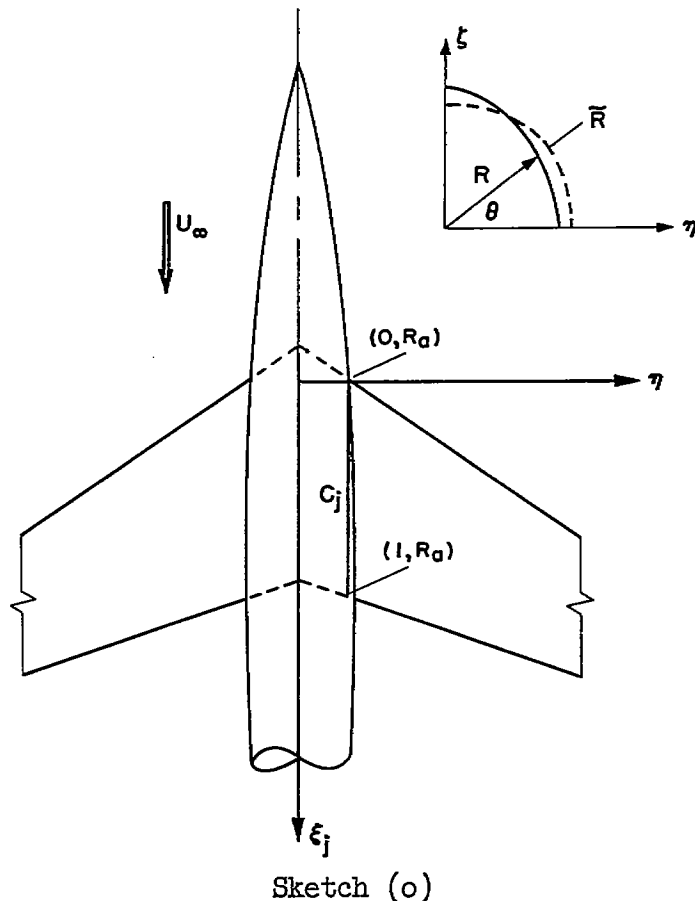
$$\Delta R'(x, \theta) = R'(x, \theta) - \bar{R}'(x)$$

Once the source and multipole strengths have been determined, the perturbation velocities may be evaluated by the use of equations (20) to (31).

#### WING-BODY COMBINATIONS

It is assumed that the wing-body combination possesses both lateral and vertical symmetry and a coordinate system is used which is dimensionless with respect to the junction chord and with origin as shown in sketch (o). The body radius is denoted by  $R$  and  $\bar{R}$  is used, when the body is non-circular, to denote the radius of an equivalent circular body having identical cross-sectional area.

The boundary condition to be satisfied at the body surface is





$$\frac{\partial R}{\partial \xi_j} + \frac{v(\theta)_w}{R} \frac{\partial R}{\partial \theta} + \frac{\partial R}{R \partial \theta} \sum_{n=2,4,\dots}^n v(\theta)_n - v(r)_w - v(r)_{n=0} - \sum_{n=2,4,\dots}^n v(r)_n = 0 \quad (94)$$

where  $v(r)_w$  and  $v(\theta)_w$  are the radial and azimuthal velocities induced by the wing (which is assumed to extend through the body from wing tip to wing tip as indicated in sketch (o)). The radial velocity induced by the axial sources is denoted by  $v(r)_{n=0}$ , and  $v(r)_n$  and  $v(\theta)_n$  represent the contributions of the axial multipoles.

The strengths of the axial sources are chosen so as to provide the required body volume or, more specifically, the body cross-sectional areas, and to eliminate the average of the wing-induced radial velocities at each axial station. The average wing-induced radial velocity is defined as

$$\left[ v(r)_w \right]_{av} = \frac{2}{\pi} \int_0^{\pi/2} v(r)_w d\theta \quad (95)$$

The strengths of the axial multipoles are chosen so as to complete the cancellation of the wing-induced radial velocities and, for non-symmetric bodies, to provide, in addition, the required distortion  $\Delta R(\xi_j, \theta) = R(\xi_j, \theta) - \tilde{R}(\xi_j)$  from the circular shape having equal area.

#### Determination of Axial Source and Multipole Strengths

Bodies having circular cross sections. - When the body shape is circular in cross section, the boundary condition at the body surface is

$$\beta \frac{\partial R}{\partial \xi_j} - \beta v(r)_w - \sum_{n=0,2,4,\dots}^n \beta v(r)_n = 0 \quad (96)$$

where the radial velocities,  $v(r)_n$ , induced by the axial sources and multipoles can be expressed in terms of the strength functions  $A_n(\xi_j)$  by the use of equations (32) and (34).

Since we are considering only symmetrical, nonlifting wings, it is possible to represent the wing-induced radial velocity by a Fourier cosine series involving only the even harmonics,

$$\beta v(r)_w = a_0(\xi_j) + a_2(\xi_j) \cos 2\theta + a_4(\xi_j) \cos 4\theta + \dots \quad (97)$$

where

$$a_0(\xi_j) = \frac{2}{\pi} \int_0^{\pi/2} \beta v(r)_w d\theta = \beta \left[ v(r)_w \right]_{av} \quad (98)$$

$$a_n(\xi_j) = \frac{4}{\pi} \int_0^{\pi/2} \beta v(r)_w \cos n\theta d\theta \quad (99)$$

thus,

$$\beta v(r)_w = \beta \left[ v(r)_w \right]_{av} + \frac{4}{\pi} \sum_{n=2,4,6,\dots}^n \cos n\theta \int_0^{\pi/2} \beta \Delta v(r)_w \cos n\theta d\theta \quad (100)$$

A consideration of equations (32), (96), and (100) leads to the following definitions for the axial source and multipole strengths:<sup>1</sup>

$$A_0 = 2\pi\beta R \left\{ \beta \frac{\partial R}{\partial \xi_j} - \beta \left[ v(r)_w \right]_{av} \right\} \quad (101)$$

$$\frac{A_n}{(\beta R)^n} = - \frac{16\beta R}{K_n} \int_0^{\pi/2} \beta \Delta v(r)_w \cos n\theta d\theta \quad (102)$$

Bodies having noncircular cross sections.— If the body shape is noncircular (but possesses both lateral and vertical symmetry), it is convenient to represent the body shape by

$$R(\xi_j, \theta) = \tilde{R}(\xi_j) + \Delta R(\xi_j, \theta) \quad (103)$$

---

<sup>1</sup>The quantity  $\Delta v(r)_w$  appearing in equations (100) and (102) can be replaced by  $v(r)_w$  if so desired.

---

where  $\Delta R$  is an even function in  $\theta$ . The axial source strengths are given by

$$\begin{aligned} A_0 &= 2\beta^2 \sqrt{\pi S_b} v(r)_0 \\ &= \beta^2 \left\{ S'_b - 2\sqrt{\pi S_b} \left[ v(r)_w \right]_{av} \right\} \end{aligned} \quad (104)$$

where  $S_b = \pi \tilde{R}^2$  is the equivalent body having equal cross-sectional area. The strengths of the axial multipoles are to be chosen so as to complete the cancellation of the wing-induced radial velocities at the body surface and to provide the required distortion  $\Delta R$  from the equivalent circular shape.

The boundary condition for determining the multipole strengths is

$$\begin{aligned} \beta \frac{\partial \Delta R}{\partial \xi_j} + \frac{\beta v(\theta)_w}{R} \frac{\partial R}{\partial \theta} - \left\{ \beta v(r)_w - \beta \left[ v(r)_w \right]_{av} \right\} - \\ \frac{1}{4\pi} \sum_{n=2,4,\dots}^n \frac{K_n A_n}{(\beta R)^{n+1}} \left( \cos n\theta - \frac{\partial R}{R \partial \theta} \sin n\theta \right) = 0 \end{aligned} \quad (105)$$

If the above equation is evaluated for a constant  $\xi_j$ , at appropriate azimuthal angles  $\theta$ , a set of simultaneous equations is obtained involving the unknown parameters  $A_n$ . If the body shape is nearly circular the azimuthal derivative  $\partial R / \partial \theta$  may be neglected, and, if the body slope is approximated according to equation (90), the multipole strengths are given approximately by

$$\frac{A_n}{(\beta R)^n} = \frac{16}{K_n} \int_0^{\pi/2} \beta \Delta R (\beta R)^{n+1} \cos n\theta \, d\theta - \frac{16\beta R}{K_n} \int_0^{\pi/2} \beta v(r)_w \cos n\theta \, d\theta \quad (106)$$

## Pressure Distributions

Once the source and multipole strength distribution functions have been determined the pressure distributions may be calculated by first obtaining the perturbation velocities and then using equation (10) or (11). At the body surface the pressure coefficient is approximately

$$C_p = -2 \left( u_w + \sum_{n=0}^n u_n \right) - \left( \frac{dR}{d\xi_j} \right)^2$$

while at the wing surface the thin-airfoil approximation can be used,

$$C_p = -2 \left( u_w + \sum_{n=0}^n u_n \right)$$

The general solutions for the perturbation velocity potential (eqs. (13) and (19)) behave properly at large distances from the wing or body, that is,

$$u, v, w \rightarrow 0$$

as the distance becomes infinitely large. The theory presented in this report can be used to calculate pressure distributions in the neighboring flow field as well as at the wing-body surface.

## ILLUSTRATIVE EXAMPLES AND COMPARISON WITH EXPERIMENT

In order to illustrate and, to a certain extent, justify the practical use of the present method for calculating pressure distributions for wing-body combinations, a comparison of some theoretical and experimental results will be presented. Because of the current interest in area-rule concepts, a comparison of theoretical and measured wing-body juncture pressures will be made for two sweptback wings of aspect ratios 3 and 6 in combination with basic Sears-Haack bodies of revolution and in combination with the basic bodies indented according to Whitcomb's transonic area rule (ref. 18). The experimental data used in the following comparison with theory were obtained in the Ames 14-foot transonic wind tunnel.

Theoretical Pressure Distributions at  $M_\infty = 0.85$  for  
an Aspect-Ratio-6 Wing in Combination With a  
Basic and Area-Rule Indented Body

The plan-form details of the aspect-ratio-6 wing in combination with a basic Sears-Haack body of fineness ratio 11 and in combination with the basic body indented according to the transonic area rule are presented in figure 2. The procedure for calculating the pressure distributions at  $M_\infty = 0.85$  will be described in detail for the indented body configuration.

Perturbation velocity components induced by the wing alone. - For this wing of large aspect ratio the taper effect is small, and the formulas given previously for determining the flow over untapered wings may be used. The flow over the wing at  $M_\infty = 0.85$  was obtained by the numerical evaluation of equations (44) to (46) using the relationships of equations (47) to (52). (A constant sweepback angle of  $\Lambda = 40^\circ$  was used.)

The locations of isobars at the wing surface are shown in figure 3. These results were obtained by use of the thin-airfoil approximation  $C_p = -2u$ . The calculated perturbation velocities at the indented body location are presented in figure 4 for several azimuthal locations (see sketch (o)). The radial component of the perturbation velocity at the body surface,

$$v(r) = v \cos \theta + w \sin \theta \quad (107)$$

and the average radial velocities, (eq. (95)), are presented in figure 5.

Determination of the axial source and multipole strength distributions. - For this configuration the body shape is circular and the axial source and multipole strengths were obtained by the use of equations (101) and (102). The variation of source strength with axial station is shown in figure 6. Equation (102) was evaluated numerically (see fig. 7 for typical variations of  $\beta \Delta v(r)_w \cos n\theta$  with  $\theta$ ) and the results for multipoles of order  $n = 2, 4$ , and  $6$  are presented in figure 8.

Wing-body juncture pressure distributions. - The streamwise perturbation velocities induced by the wing planar sources, axial sources, and axial multipoles of order  $n = 2, 4$ , and  $6$  for the aspect-ratio-6 wing in combination with the indented and basic bodies are shown in figures 9 and 10. The difference in the flow fields about the two configurations is primarily the result of differences in the strength distribution of axial sources (see also fig. 6). The influence of the axial multipoles on the flow field is comparatively small and decreases rapidly with an increase in the order  $n$  of the multipole.

A direct comparison of theoretical wing-body juncture pressure distributions for the basic and indented bodies is presented in figure 11. Also included in figure 11 is the theoretical pressure distribution at the wing mid-semispan (which is sufficiently far removed from the model center line and wing tip so as to be essentially free of end effects in subsonic flows). For the indented body the juncture pressure distribution is almost identical with the pressure distribution of the mid-semispan. Additional calculations at other spanwise stations indicate that the isobar pattern on the wing for the indented combination (excluding the local regions near the wing tips) is essentially two-dimensional, that is, the isobars tend to follow the local sweep lines of the wing.

### Comparison With Experiment

A comparison of some theoretical and measured pressure coefficients at  $M_\infty = 0.85$  for the aspect-ratio-6 wing in combination with the indented and basic bodies is presented in figures 12 and 13. The comparison of theory and experiment is made for two body azimuthal locations,<sup>2</sup>  $\theta = 0^\circ$  and  $\theta = 90^\circ$ . The measured pressures at a row of wing orifices in the immediate vicinity of the body (see fig. 2) are also included in figures 12 and 13 since it was felt that a comparison of theory and experiment at the wing-body junction would suffer somewhat from boundary-layer effects in the corners of the wing-body juncture. In general, the theory and experiment are in reasonably good agreement.

Similar comparisons of theory and experiment for the aspect-ratio-3 wing and body combinations shown in figure 14 are presented in figures 15 and 16. For this case the perturbation velocities induced by the wing alone were evaluated by numerical means using the theory for wings of tapered plan form. The location of isobars at the wing surface are shown in figure 17. A convenient formula for obtaining the variation of the local sweepback angle with junction-chord station  $\xi_j$  is

$$\tan \Lambda_e(\xi_j) = \tan \Lambda_e(0) - \frac{\xi_j K_\Lambda}{\beta} \quad (108)$$

---

<sup>2</sup>At the wing-body juncture the pressure orifices along the sides of the bodies were located as close as possible to the upper surface of the wing. The designation  $\theta = 0^\circ$  for the side row of orifices is used here for convenience, although, at the wing-body juncture, the orifice locations differed slightly from  $\theta = 0^\circ$  because of the finite thickness of the wing.

---

## CONCLUDING REMARKS

In this report a theoretical method has been developed for determining the linearized subsonic flow about symmetrical, nonlifting wing-body combinations. Particular emphasis has been placed on developing practical methods for use in obtaining numerical results. As part of the present analysis a theory was developed for determining the flow about noncircular bodies by the use of axially distributed sources and multipoles. The flow over thin, nonlifting airfoils having symmetrical profiles was also studied in considerable detail and it was shown that the concept of the oblique source filament could be used for wings having tapered as well as untapered plan forms. This is of considerable importance since numerical results can be obtained for the tapered wing almost as easily as for the untapered wing.

Ames Aeronautical Laboratory  
National Advisory Committee for Aeronautics  
Moffett Field, Calif., Feb. 5, 1957

## REFERENCES

1. Munk, Max M.: The Aerodynamic Forces on Airship Hulls. NACA Rep. 184, 1924.
2. Jones, Robert T.: Properties of Low-Aspect-Ratio Pointed Wings at Speeds Below and Above the Speed of Sound. NACA Rep. 835, 1946.
3. Ward, G. N.: Supersonic Flow Past Slender Pointed Bodies. Quart. Jour. Mech. and Appl. Math., vol. II, pt. 1, 1949, pp. 75-97.
4. Adams, Mac. C., and Sears, W. R.: Slender-Body Theory - Review and Extension. Jour. Aero. Sci., vol. 20, no. 2, Feb. 1953, pp. 85-98.
5. Heaslet, Max. A., and Lomax, Harvard: The Calculation of Pressure on Slender Airplanes in Subsonic and Supersonic Flow. NACA TN 2900, 1953.
6. Byrd, Paul F.: Theoretical Pressure Distribution for Some Slender Wing-Body Combinations at Zero Lift. NACA TN 3674, 1956.
7. Göthert, B.: Plane and Three-Dimensional Flow at High Subsonic Speeds. NACA TM 1105, 1946.
8. Van Dyke, Milton D.: A Study of Second-Order Supersonic-Flow Theory. NACA Rep. 1081, 1952. (Supersedes NACA TN 2200)

9. Lamb, Horace: Hydrodynamics. Sixth ed., Dover Pub., 1945.
10. Jones, Robert T.: Thin Oblique Airfoils at Supersonic Speeds. NACA TN 1107, 1946.
11. Jones, Robert T.: Subsonic Flow Over Thin Oblique Airfoils at Zero Lift. NACA Rep. 902, 1948.
12. Neumark, Stefan: Velocity Distribution on Straight and Sweptback Wings of Small Thickness and Infinite Aspect Ratio at Zero Incidence. R.A.E. Rep. Aero. 2200, May 1947.
13. Küchemann, D.: Design of Wing Junction, Fuselage and Nacelles to Obtain the Full Benefit of Sweptback Wings at High Mach Number. R.A.E. Rep. Aero. 2219, Oct. 1947.
14. Jones, Robert T.: Wing Plan Forms for High-Speed Flight. NACA Rep. 863, 1947. (Supersedes NACA TN 1033)
15. Weber, J.: The Calculation of the Pressure Distribution Over the Surface of Two-Dimensional and Swept Wings with Symmetrical Aerofoil Sections. R.A.E. Rep. Aero. 2497, July 1953.
16. Neumark, S., and Collingbourne, J.: Velocity Distribution on Thin Tapered Wings with Fore-And-Aft Symmetry and Spanwise Constant Thickness Ratio at Zero Incidence. R.A.E. Rep. Aero. 2432, June 1951.
17. Neumark, S., and Collingbourne, J.: Velocity Distribution on Thin Tapered Arrowhead and Delta Wings with Spanwise Constant Thickness Ratio at Zero Incidence. Appendix - Computation of Supercriticality on A.C.E. by E. J. York. R.A.E. Rep. Aero. 2545, May 1955.
18. Whitcomb, Richard T.: A Study of the Zero-Lift Drag-Rise Characteristics of Wing-Body Combinations Near the Speed of Sound. NACA RM L52H08, 1952.





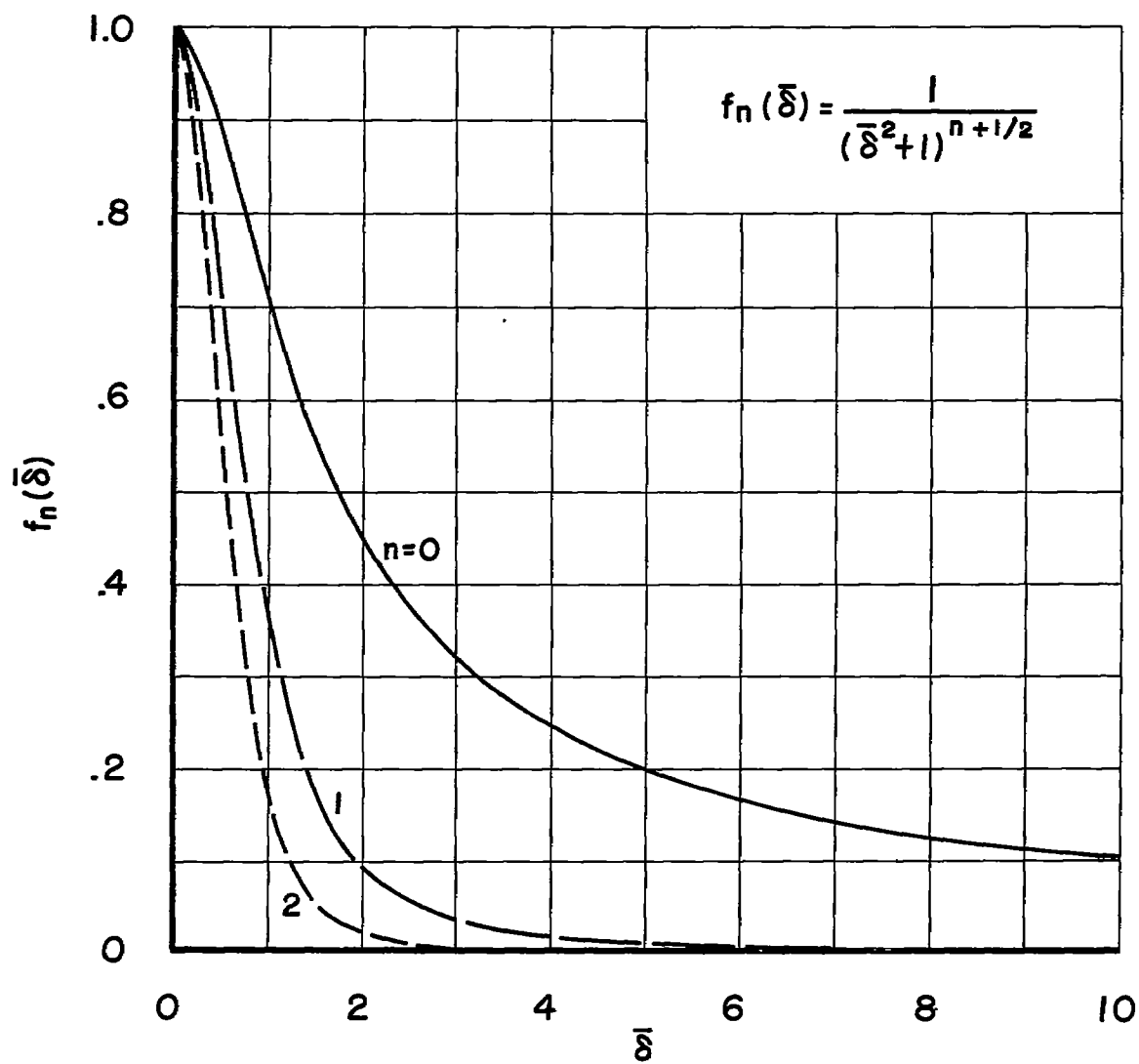
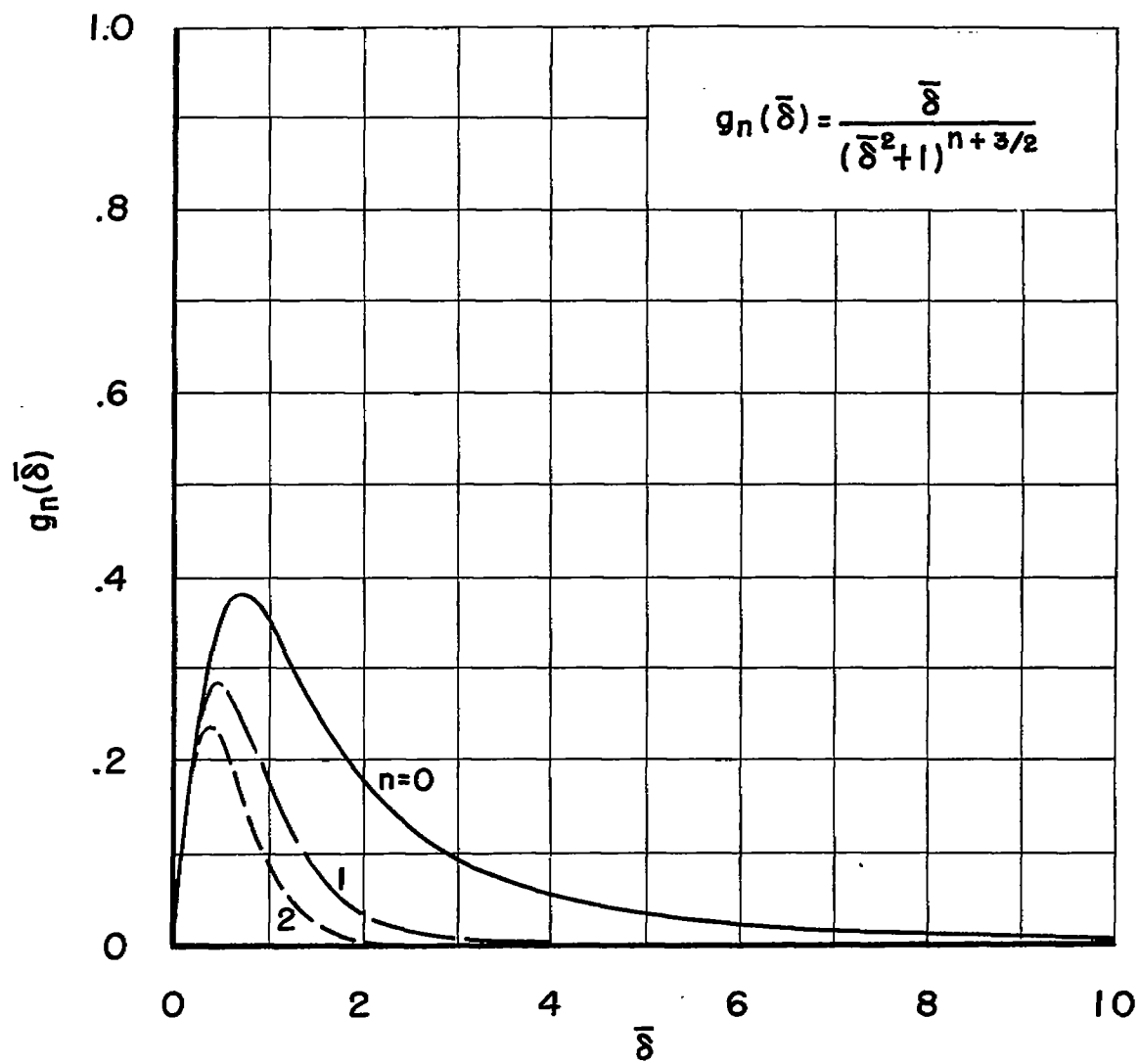
(a)  $f_n(\bar{\delta})$ 

Figure 1.- The variations of the multipole influence functions  $f_n$ ,  $g_n$ , and  $h_n$  with  $\bar{\delta}$ .



(b)  $g_n(\bar{\delta})$

Figure 1.- Continued.

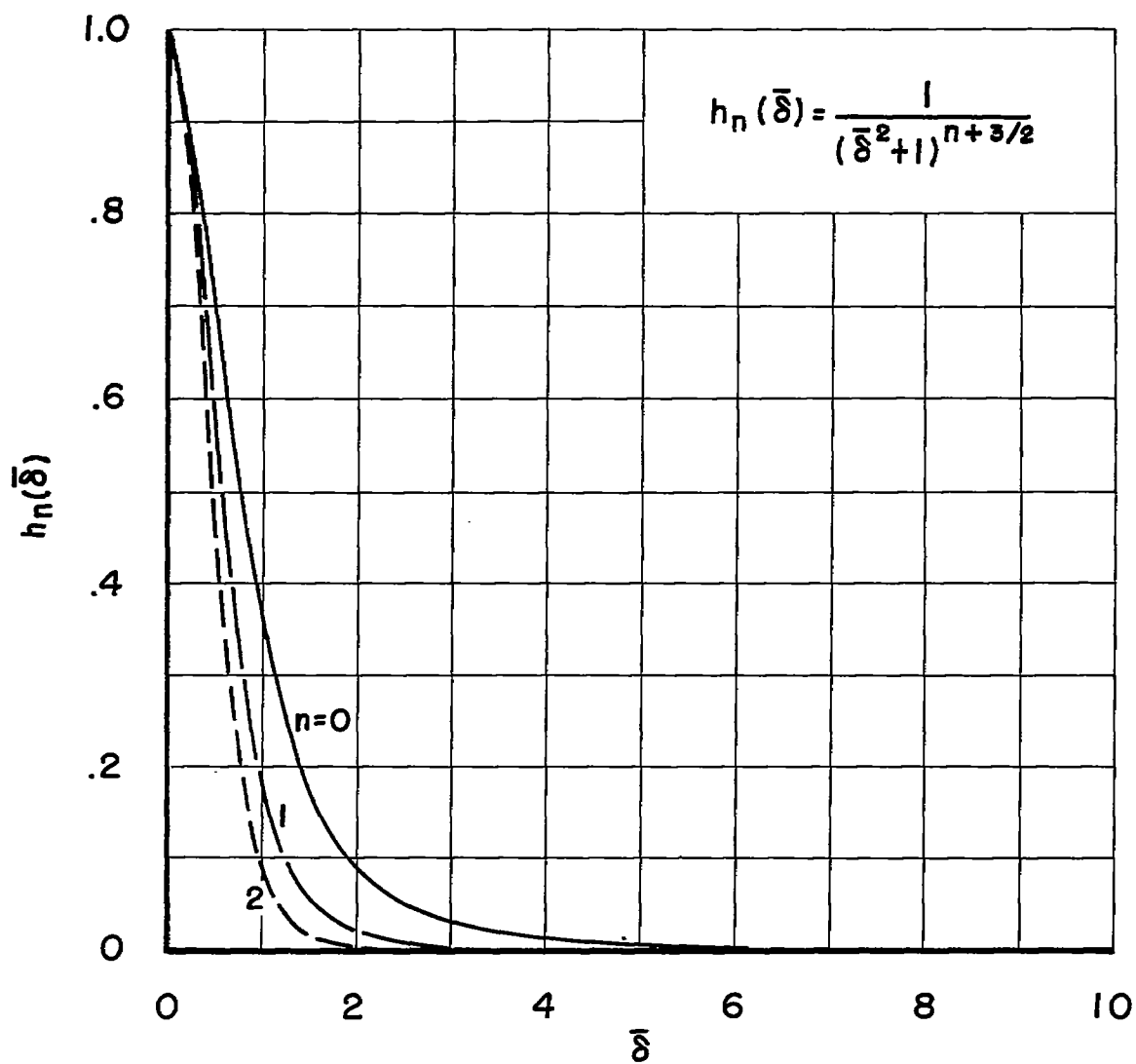
(c)  $h_n(\bar{\delta})$ 

Figure 1.- Concluded.

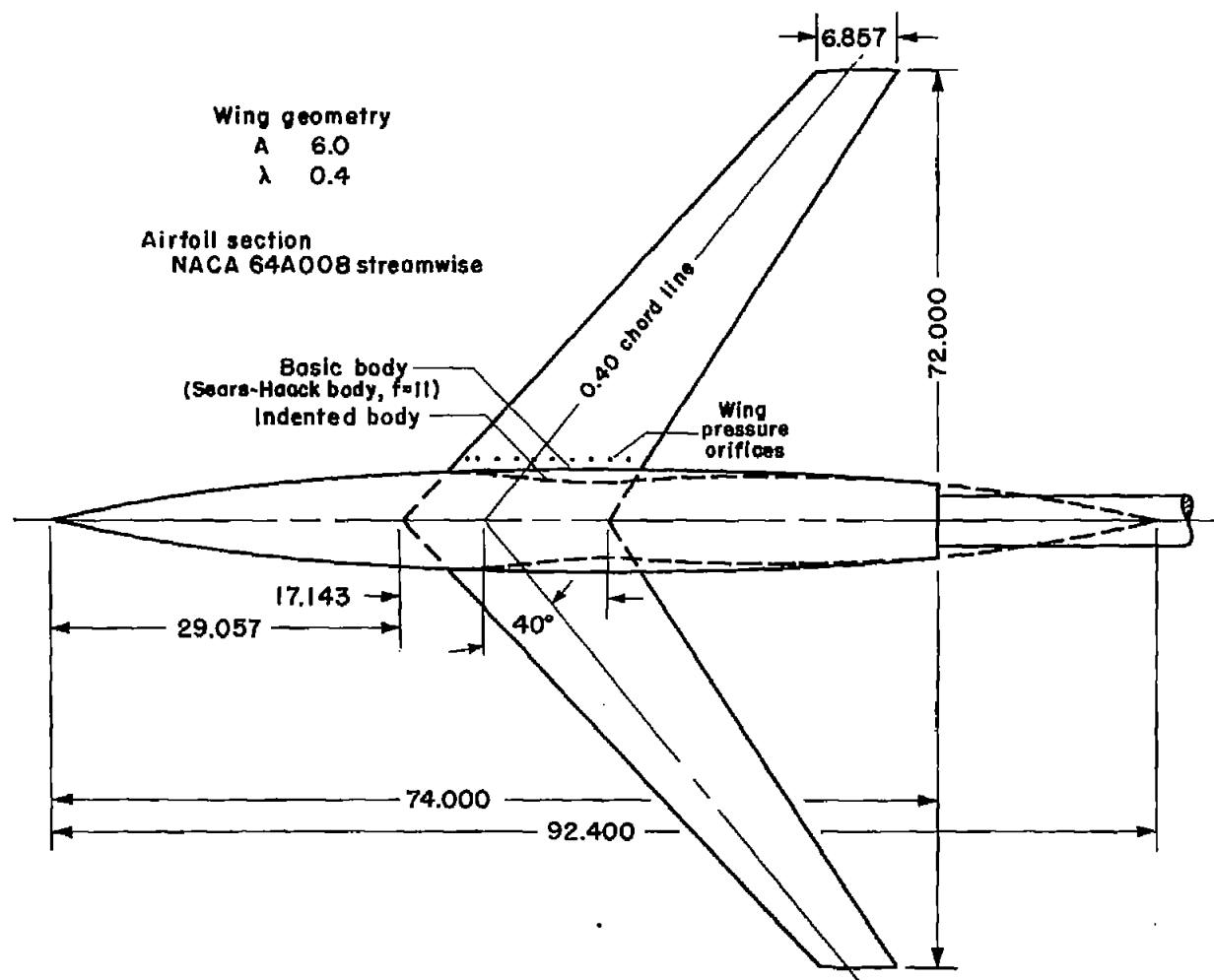


Figure 2.- Plan-form details of the aspect-ratio-6 wing in combination with a basic Sears-Haack body and an indented body.

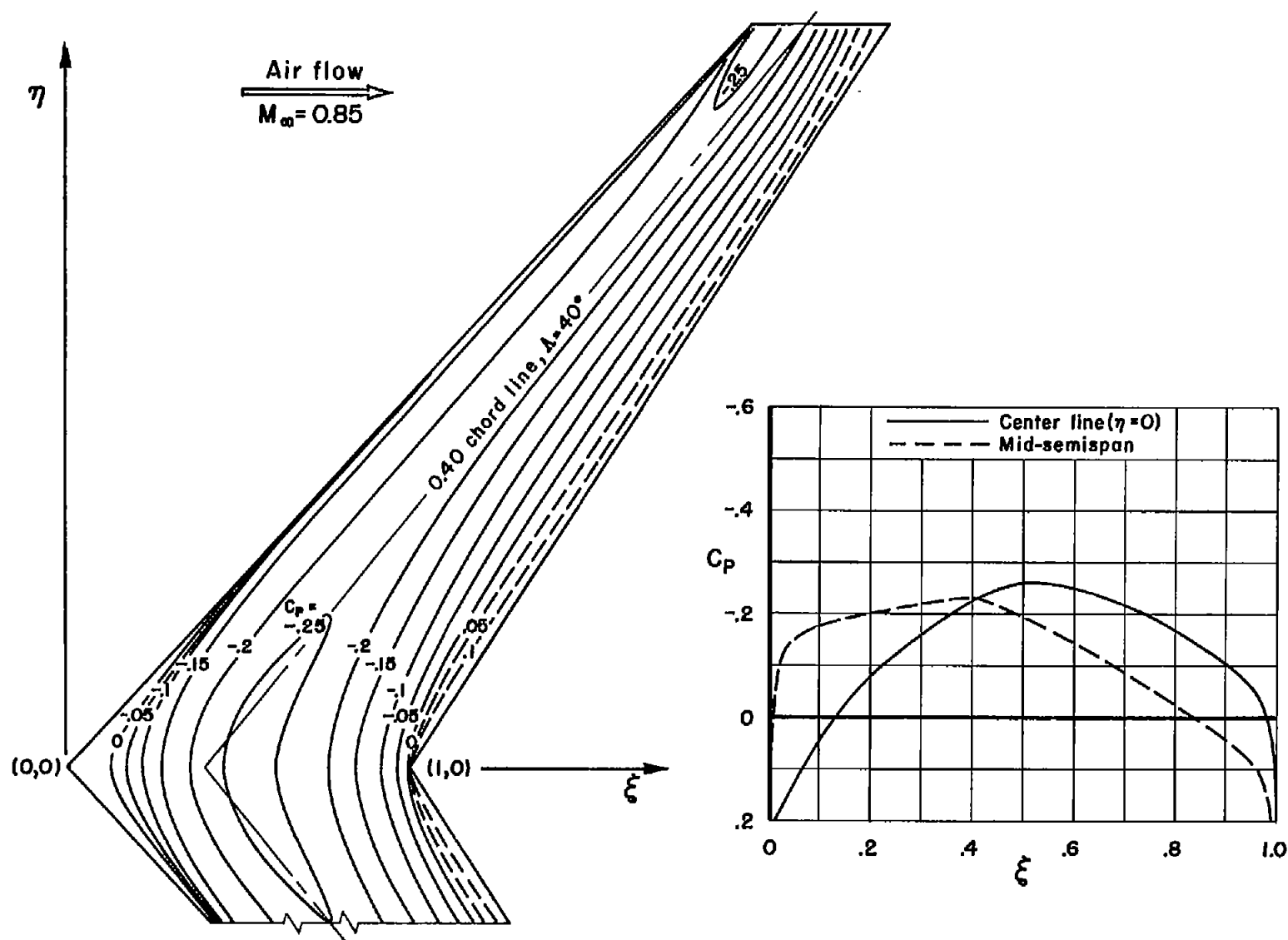


Figure 3.- Isobars at the upper surface of the aspect-ratio-6 wing.

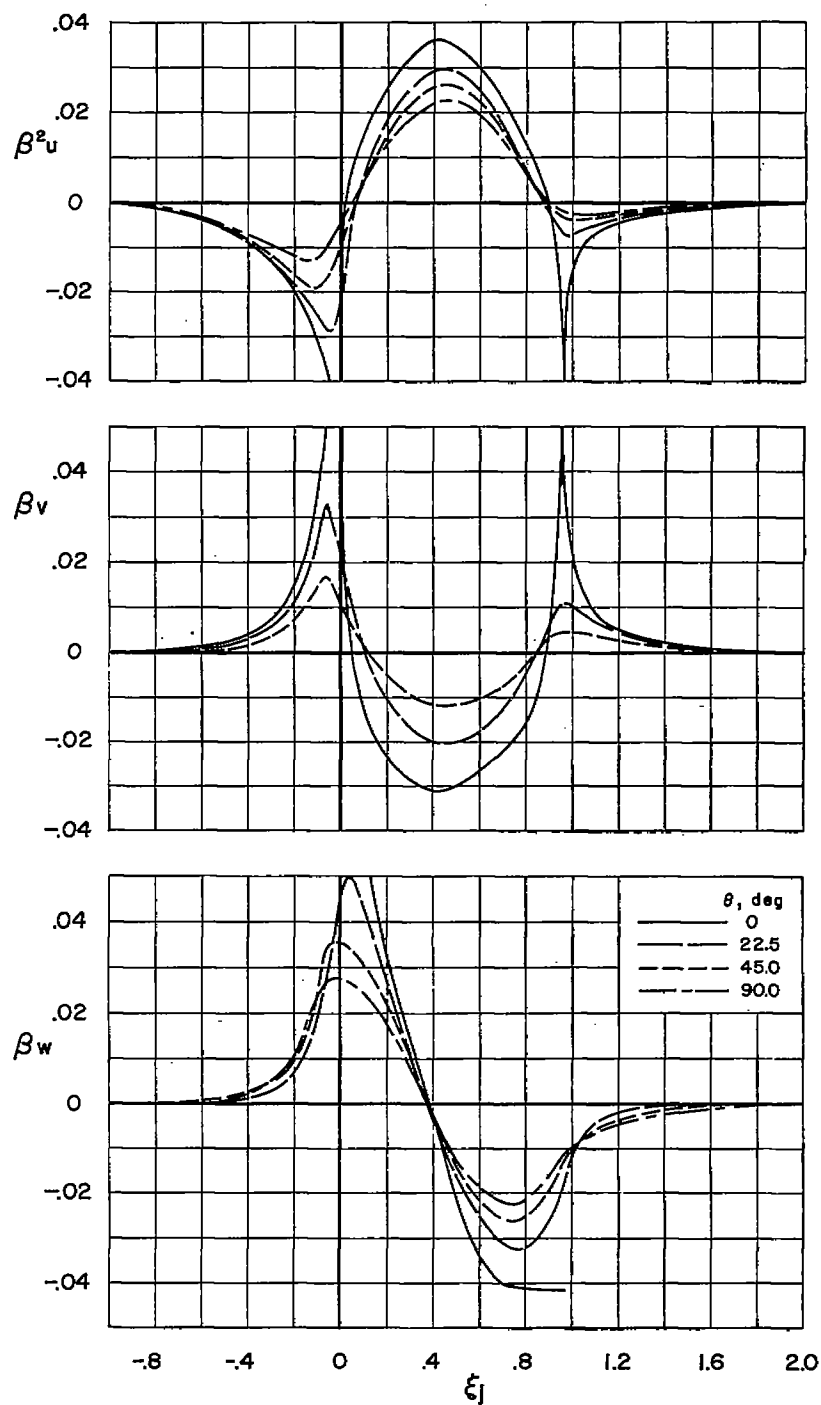


Figure 4.- Wing-induced perturbation velocities at the area-rule body;  
 $M_\infty = 0.85$ .

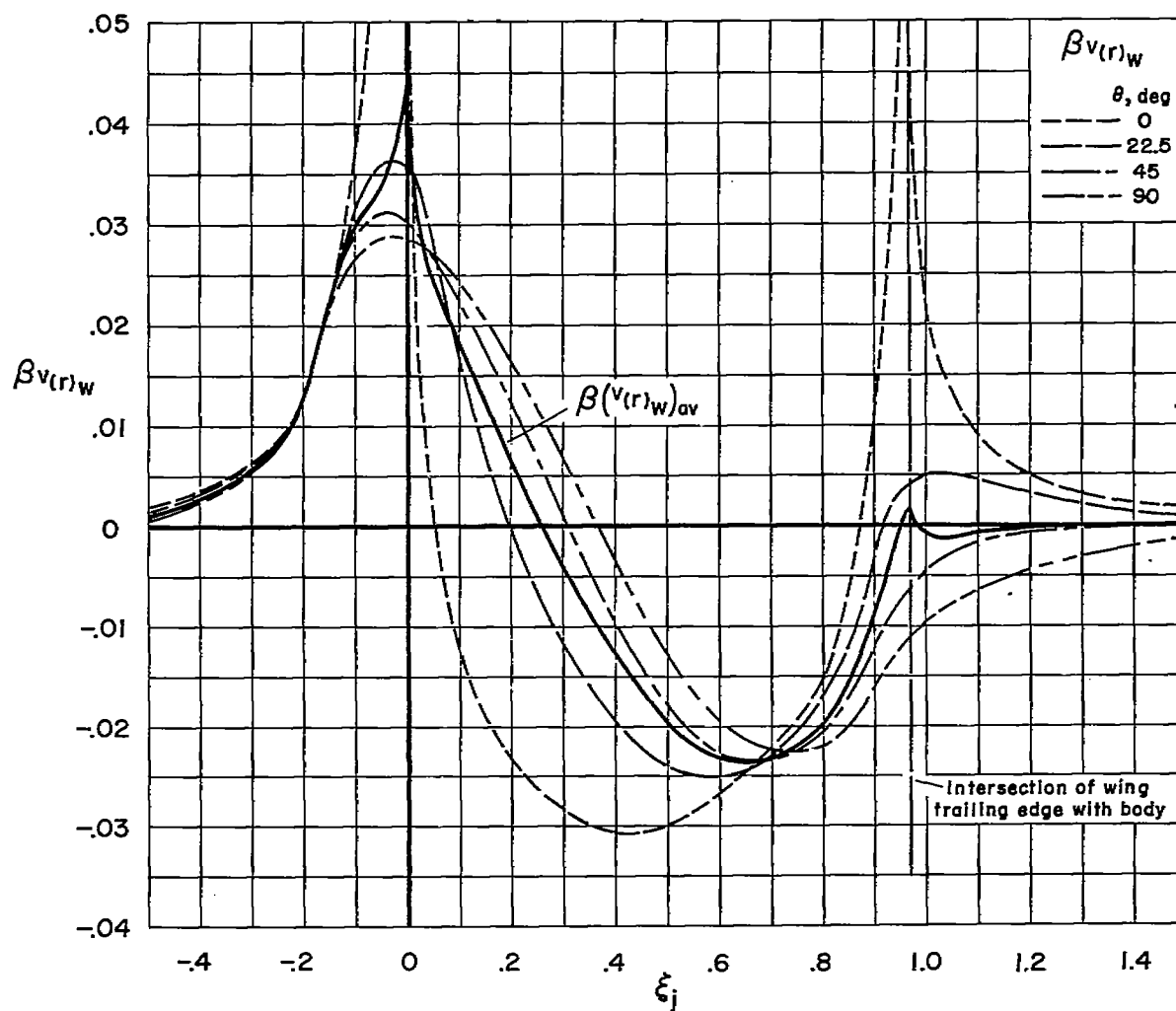


Figure 5.- Wing-induced radial velocities at the area-rule body;  
 $M_\infty = 0.85$ .



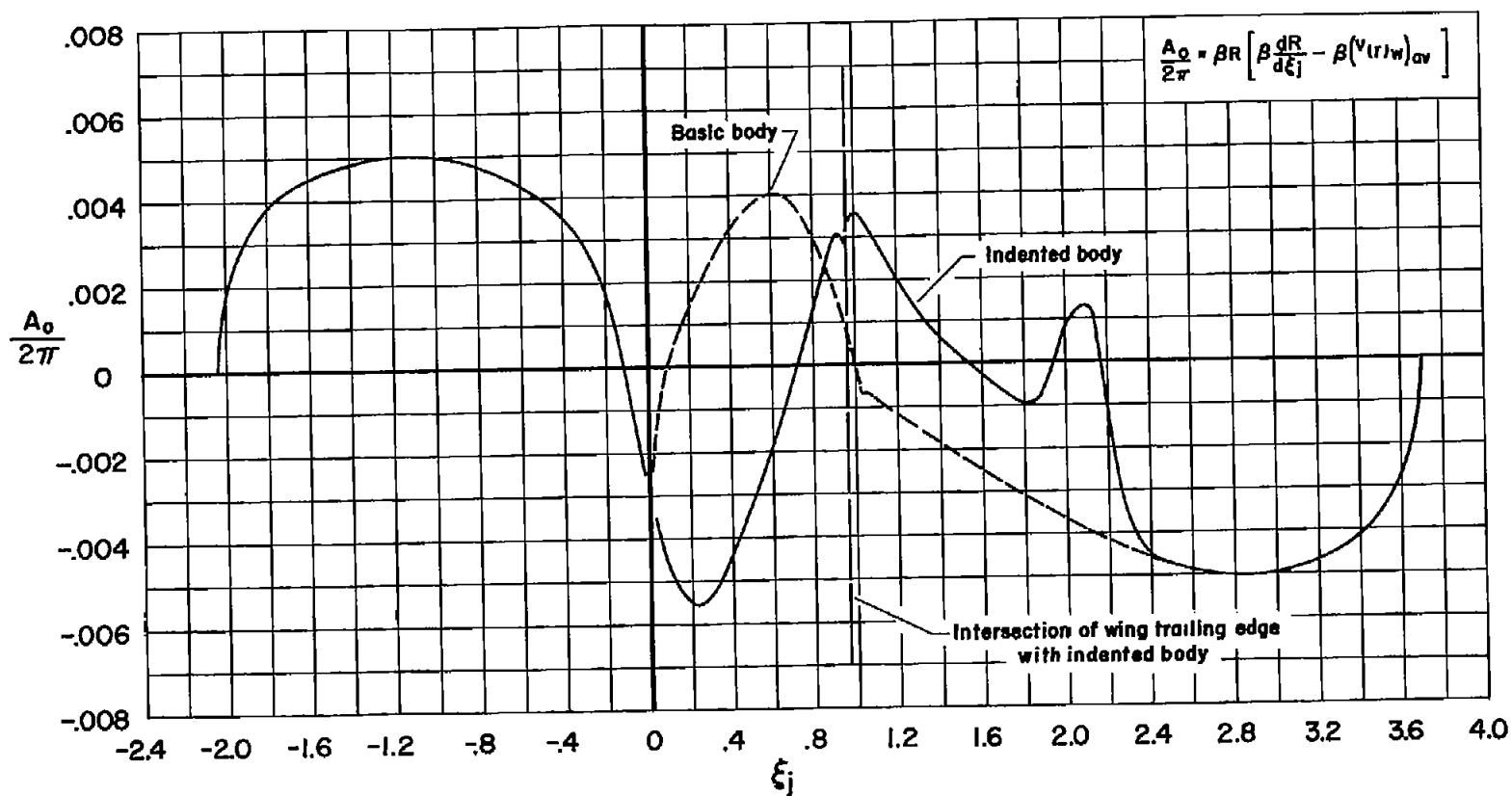


Figure 6.- The variation of axial source strength with junction-chord station  $\xi_j$ .

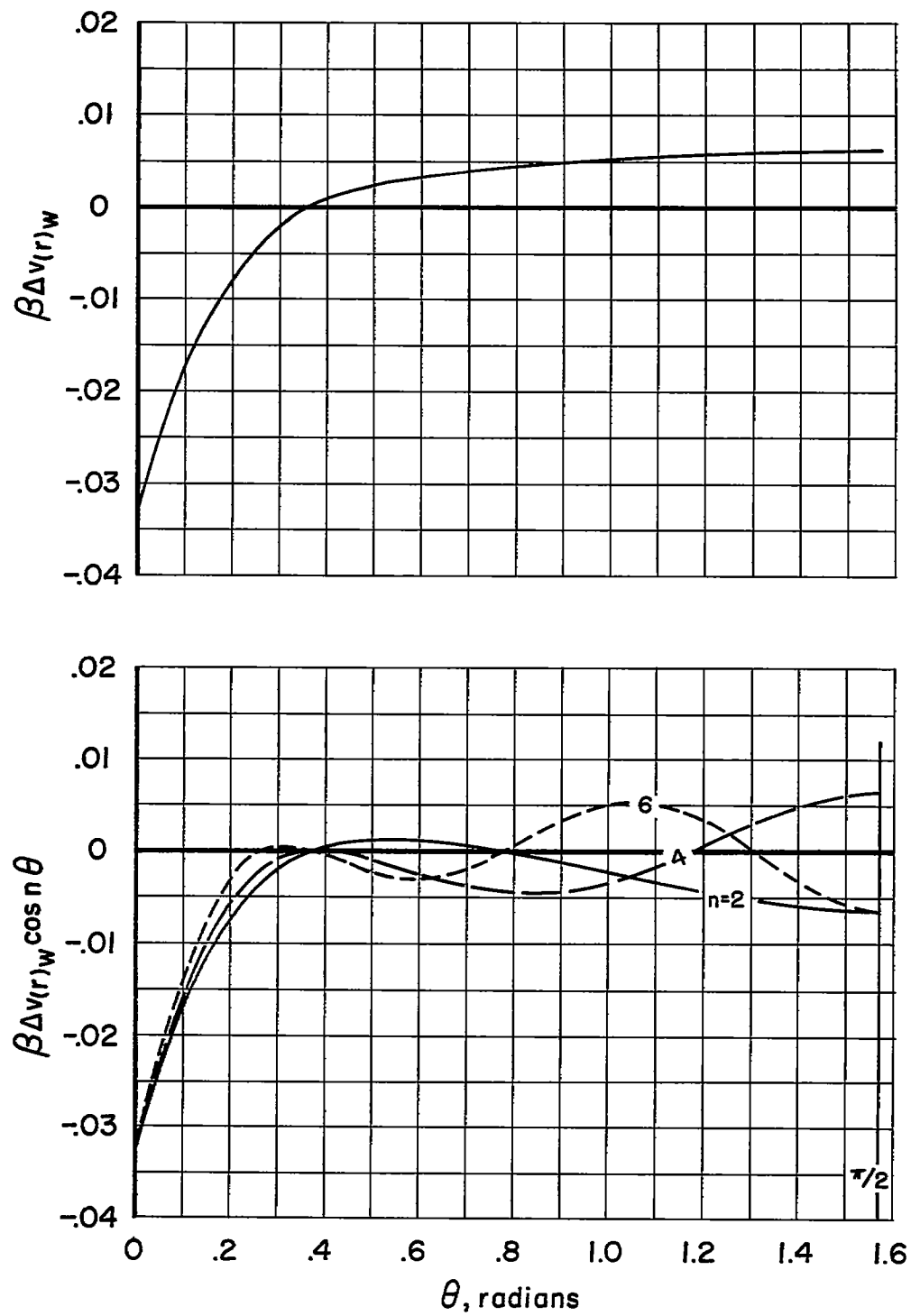


Figure 7.- The variations of  $\beta \Delta v(r)_w$  and  $\beta \Delta v(r)_w \cos n\theta$  with  $\theta$  for  $\xi_j = 0.1$ .

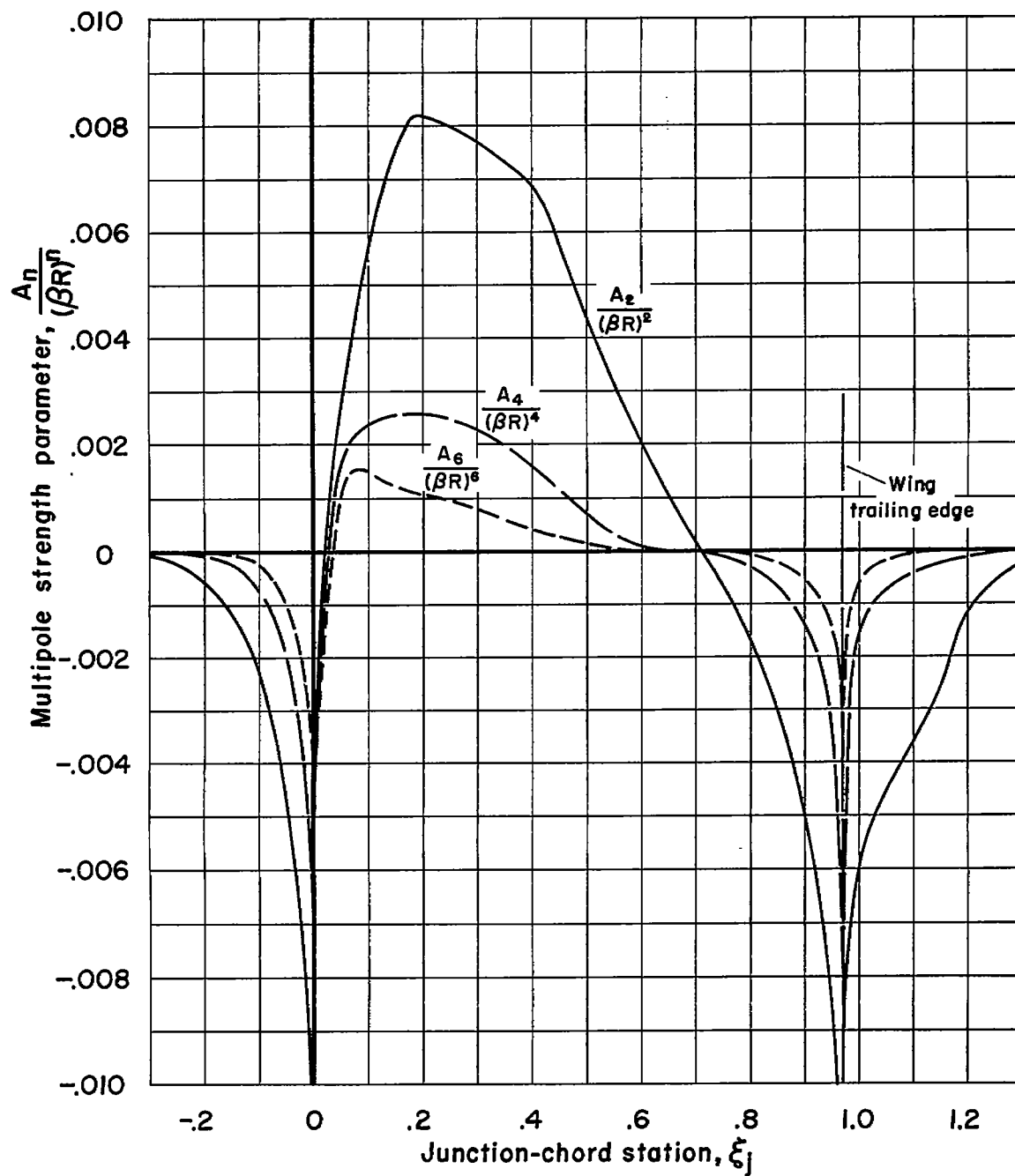


Figure 8.- The variations of the axial multipole strength parameters  $A_n/(\beta R)^n$  with junction-chord station  $\xi_j$ .

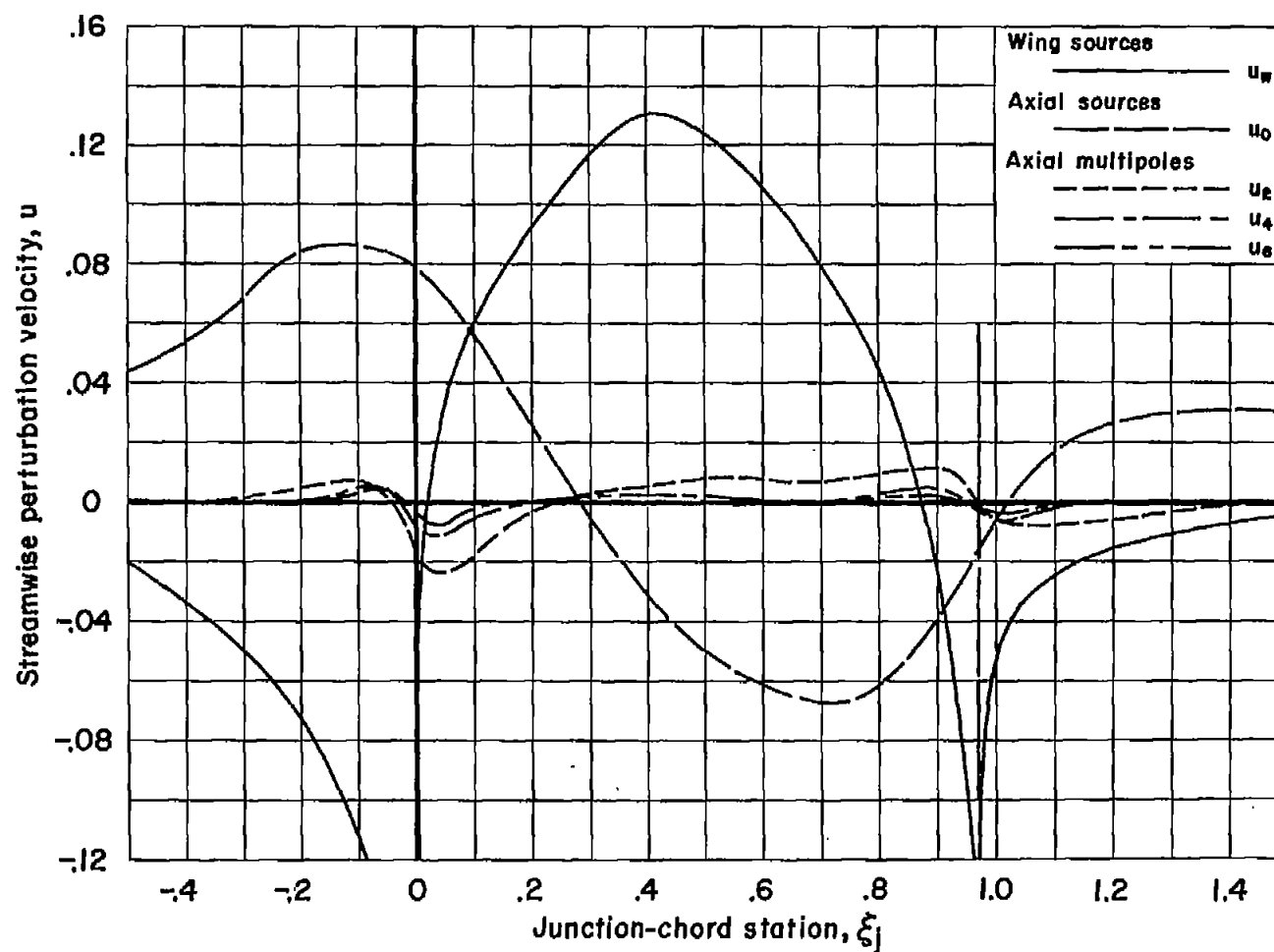


Figure 9.- The streamwise perturbation velocities induced at the wing-body juncture by the wing sources, axial sources, and axial multipoles for the aspect-ratio-6 wing in combination with the indented body;  $M_\infty = 0.85$ .

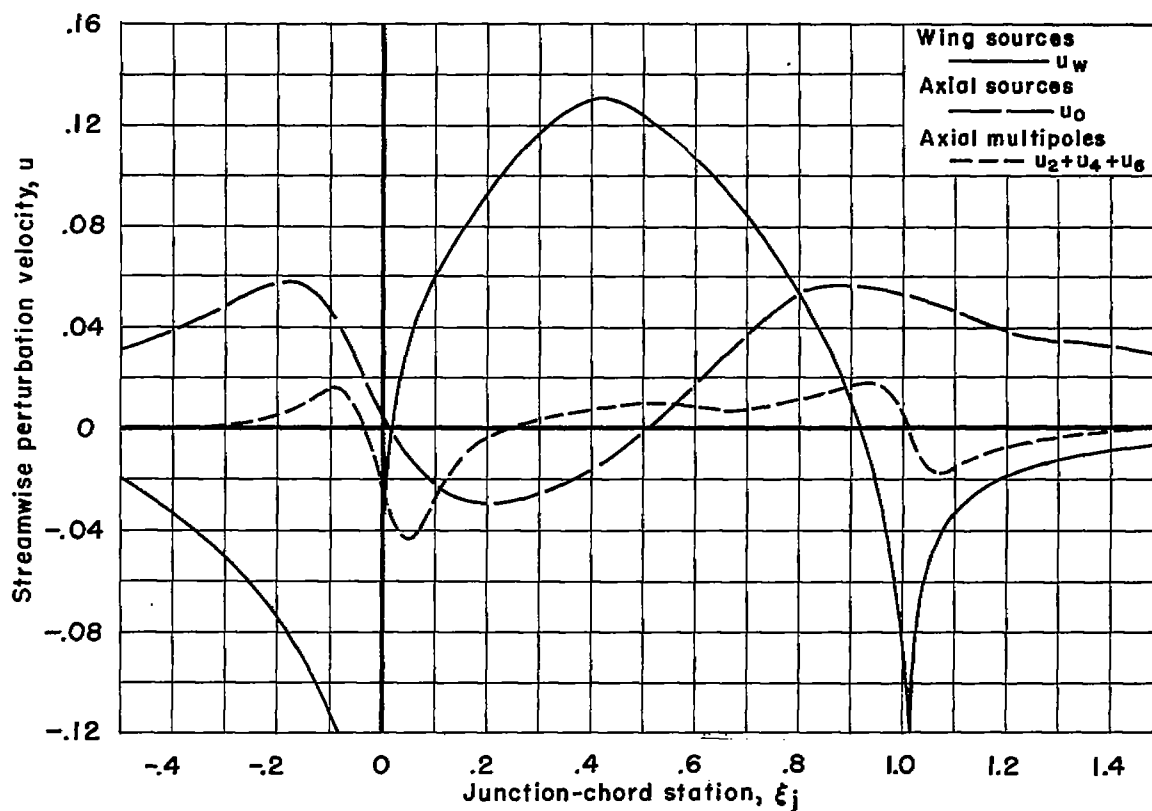


Figure 10.- The streamwise perturbation velocities induced at the wing-body juncture by the wing sources, axial sources, and axial multipoles for the aspect-ratio-6 wing in combination with the basic body;  
 $M_\infty = 0.85$ .

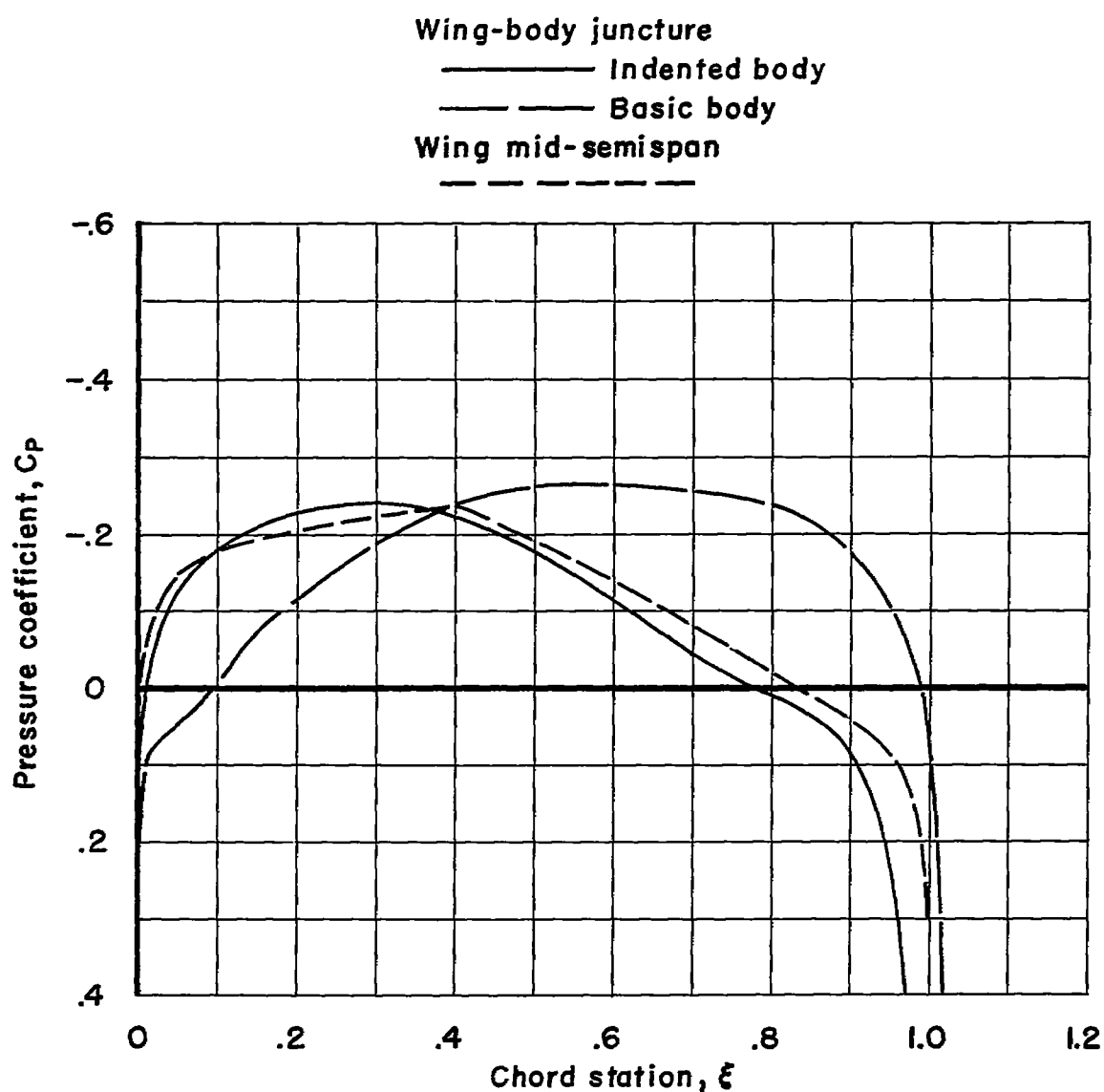


Figure 11.- A comparison of calculated pressure coefficients at the wing-body junctures of the aspect-ratio-6 wing in combination with the basic and indented bodies;  $M_\infty = 0.85$ .

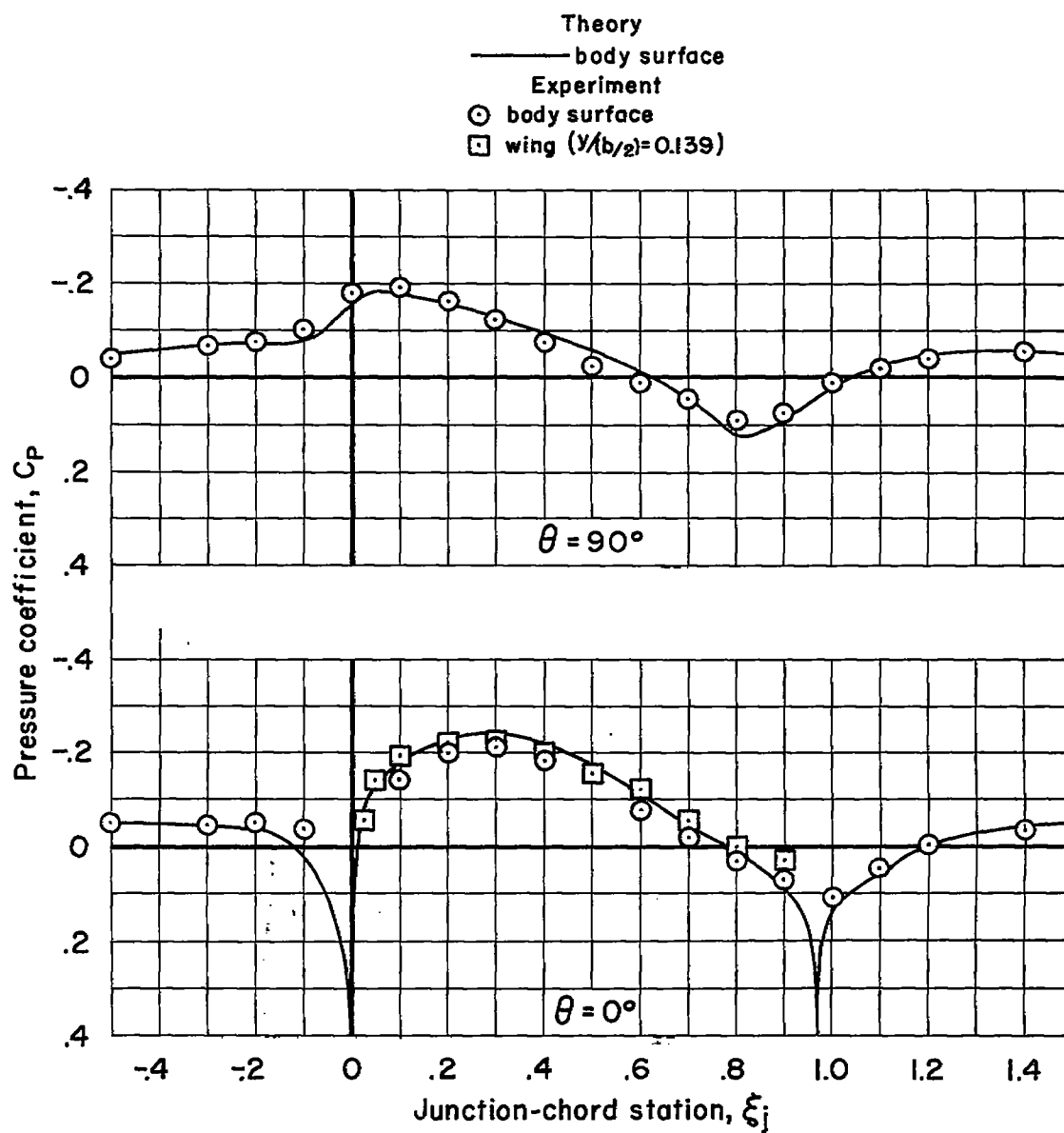


Figure 12.- A comparison of theoretical and measured pressure coefficients at  $M_\infty = 0.85$  for the aspect-ratio-6 wing in combination with an area rule indented body.

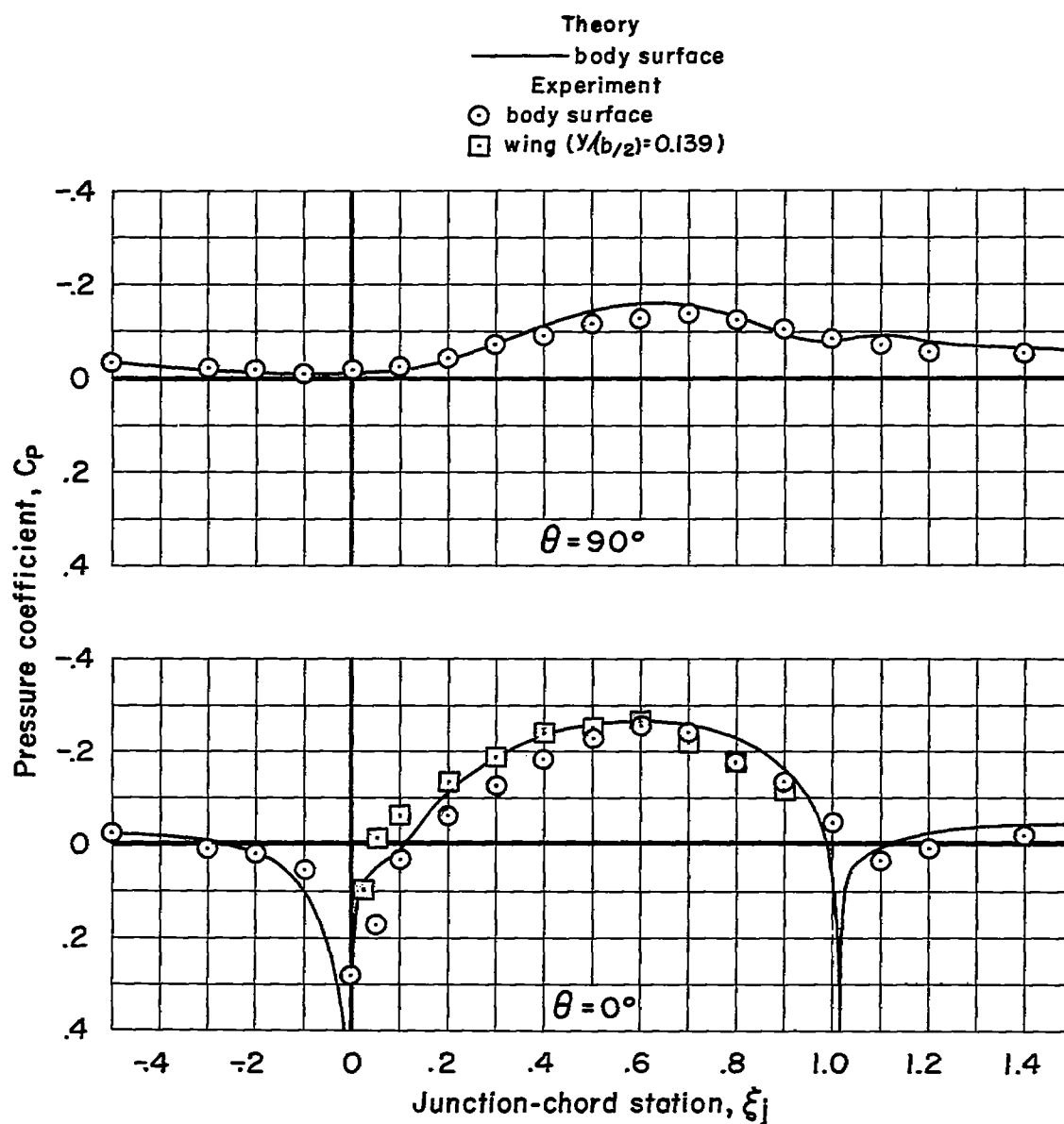


Figure 13.- A comparison of theoretical and measured pressure coefficients at  $M_\infty = 0.85$  for the aspect-ratio-6 wing in combination with a Sears-Haack body.



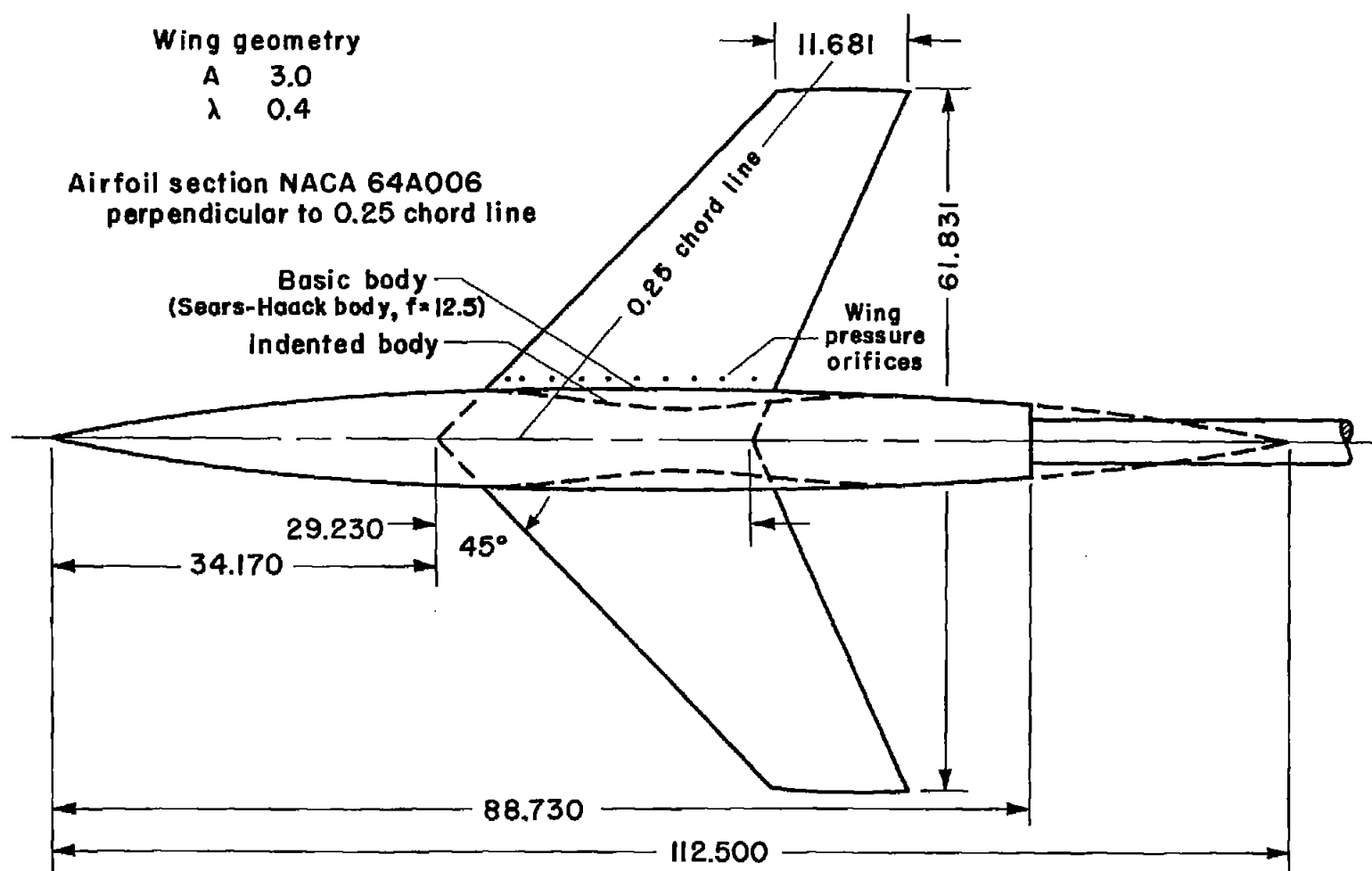


Figure 14.- Plan-form details of the aspect-ratio-3 wing in combination with a basic Sears-Haack body and an indented body.

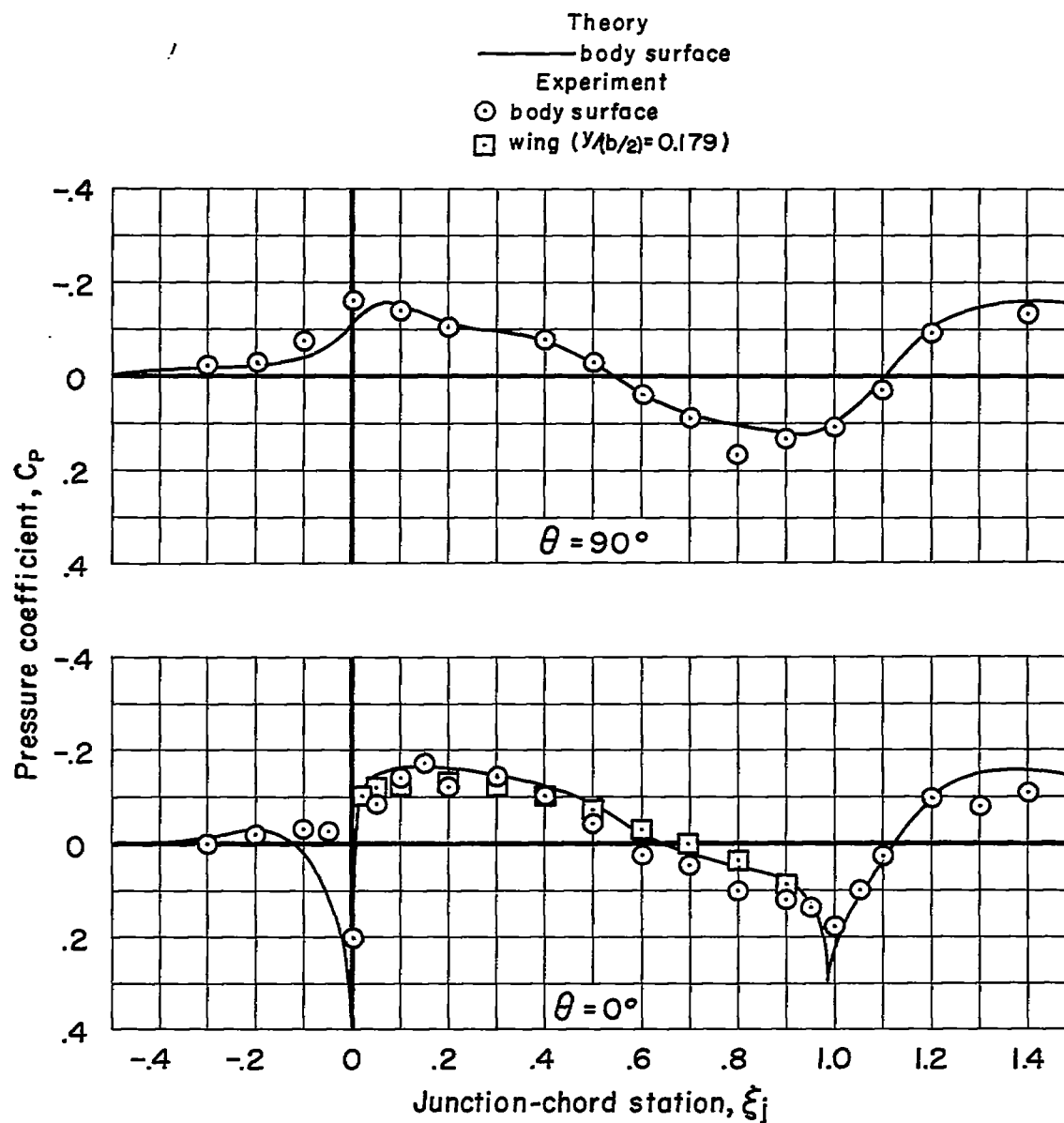


Figure 15.- A comparison of theoretical and measured pressure coefficients at  $M_\infty = 0.85$  for the aspect-ratio-3 wing in combination with an area rule indented body.

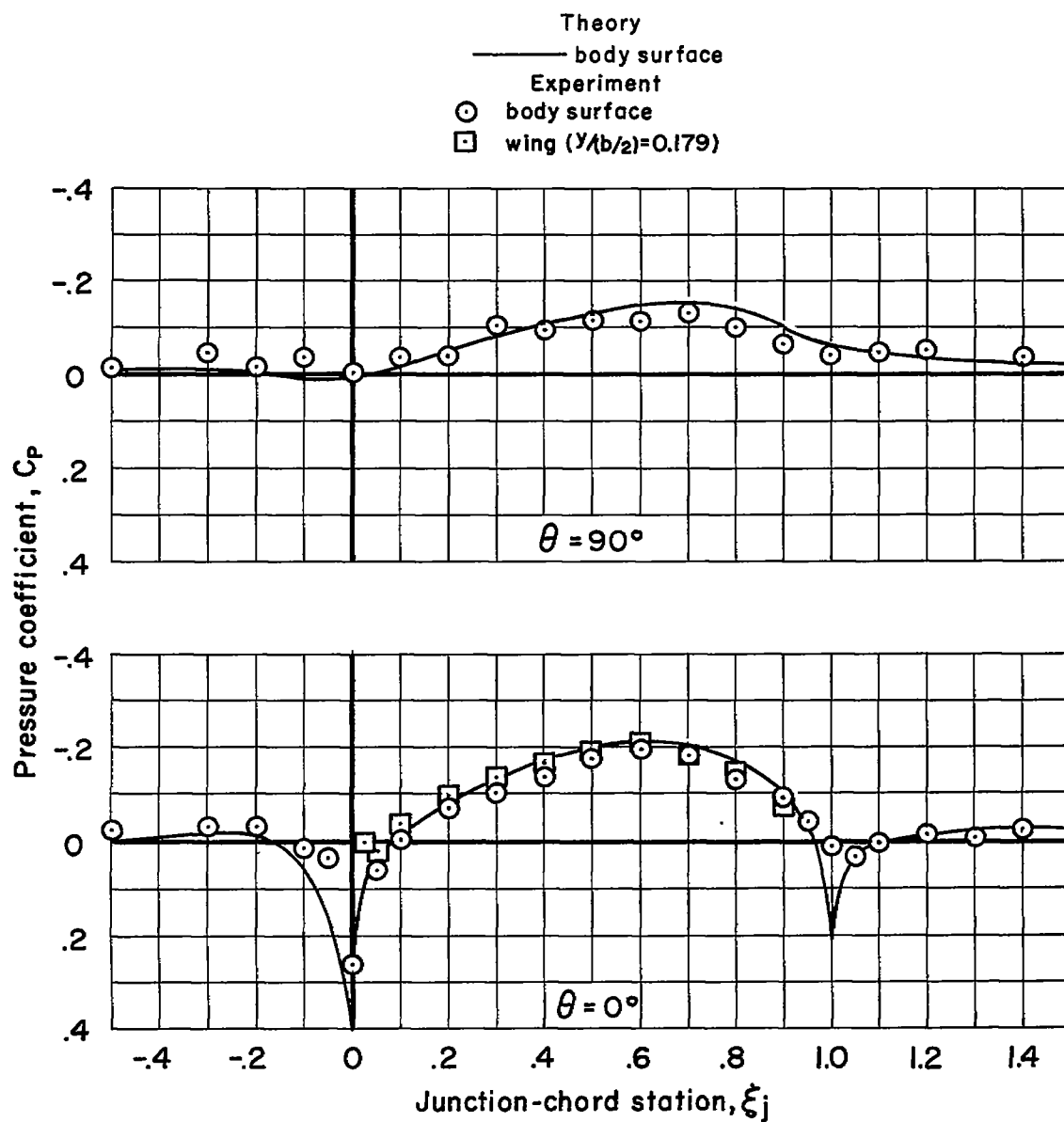


Figure 16.- A comparison of theoretical and measured pressure coefficients at  $M_\infty = 0.85$  for the aspect-ratio-3 wing in combination with a Sears-Haack body.

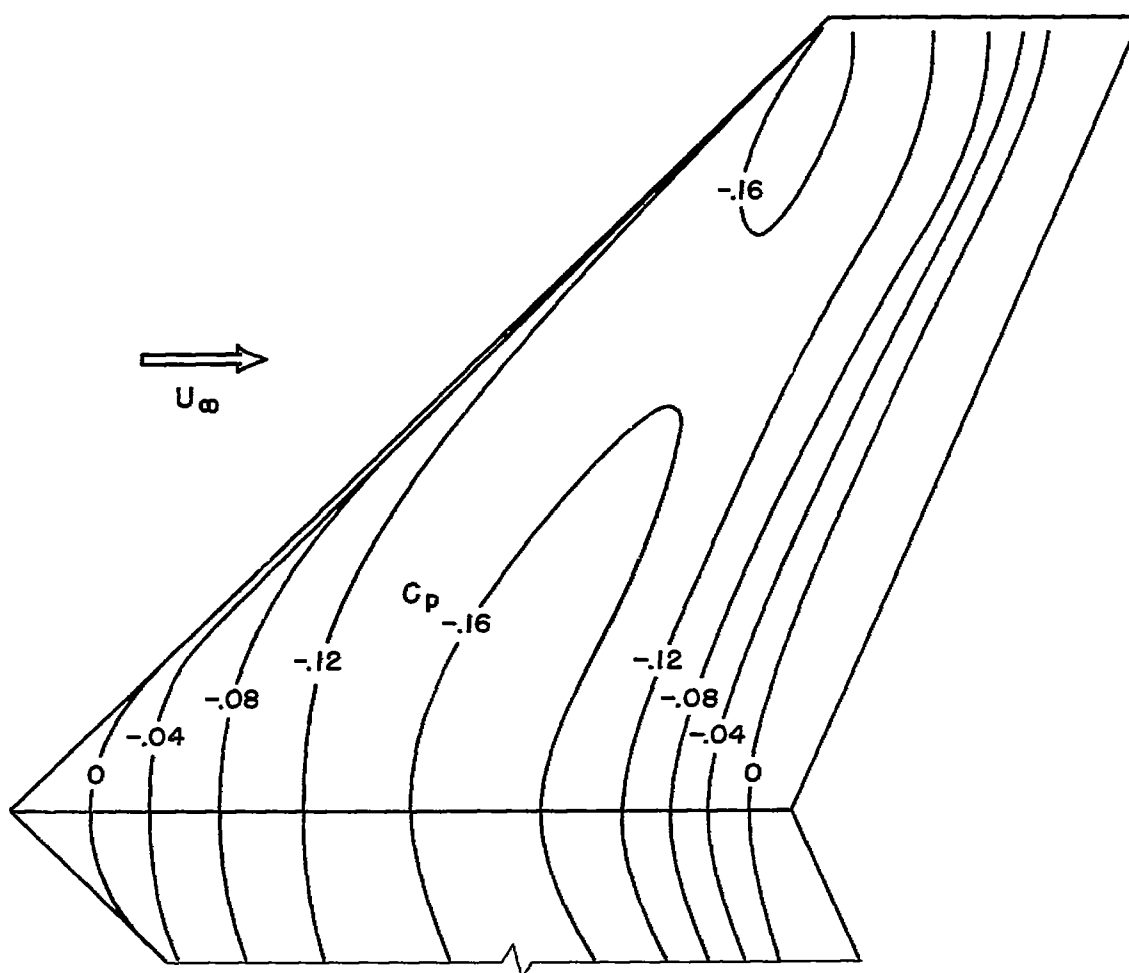


Figure 17.- Isobars for the aspect-ratio-3 wing;  $M_\infty = 0.85$ .